Validation of 13 Hot and Potentially Terrestrial TESS Planets

Steven Giacalone[1], Courtney D. Dressing[1], Christina Hedges[2,3], Veselin B. Kostov[4,5], Karen A. Collins[6],
Eric L. N. Jensen[7], Daniel A. Yahalomi[6,8], Allyson Bieryla[6], David R. Ciardi[9], Steve B. Howell[3], Jorge Lillo-Box[10],
Khalid Barkaoui[11,12], Jennifer G. Winters[6], Elisabeth Matthews[13], John H. Livingston[14], Samuel N. Quinn[6],
Boris S. Safonov[15], Charles Cadieux[16,78], E. Furlan[9], Ian J. M. Crossfield[17], Avi M. Mandell[4],
Emily A. Gilbert[4,18,19,20,21], Ethan Kruse[4], Elisa V. Quintana[4], George R. Ricker[22], S. Seager[22,23,24],
Joshua N. Winn[25], Jon M. Jenkins[3], Britt Duffy Adkins[26], David Baker[27], Thomas Barclay[4,19], David Barrado[10],
Natalie M. Batalha[28], Alexander A. Belinski[15], Zouhair Benkhaldoun[29], Lars A. Buchhave[30], Luca Cacciapuoti[31,32],
David Charbonneau[6], Ashley Chontos[33,76], Jessie L. Christiansen[9], Ryan Cloutier[6,77], Kevin I. Collins[34],
Dennis M. Conti[35], Neil Cutting[27], Scott Dixon[36], René Doyon[16,78], Mohammed El Mufti[37,38],
Emma Esparza-Borges[39,40], Zahra Essack[23,41], Akihiko Fukui[38,42], Tianjun Gan[43], Kaz Gary[17], Mourad Ghachoui[11,29],
Michaël Gillon[11], Eric Girardin[44], Ana Glidden[22,23], Erica J. Gonzales[45,76], Pere Guerra[46], Elliott P. Horch[47],
Krzysztof G. Hełminiak[48], Andrew W. Howard[49], Daniel Huber[33], Jonathan M. Irwin[6], Giovanni Isopi[50],
Emmanuël Jehin[11], Taiki Kagetani[51], Stephen R. Kane[52], Kiyoe Kawauchi[39], John F. Kielkopf[53], Pablo Lewin[54],
Lindy Luker[27], Michael B. Lund[9], Franco Mallia[50], Shude Mao[42,55], Bob Massey[56], Rachel A. Matson[57],
Ismael Mireles[58], Mayuko Mori[59], Felipe Murgas[39,40], Norio Narita[39,42,60], Tanner O'Dwyer[27], Erik A. Petigura[26],
Alex S. Polanski[17], Francisco J. Pozuelos[11,61], Enric Palle[39,40], Hannu Parviainen[39,40], Peter P. Plavchan[37],
Howard M. Relles[6], Paul Robertson[62], Mark E. Rose[3], Pamela Rowden[63], Arpita Roy[64,65], Arjun B. Savel[66],
Joshua E. Schlieder[4], Chloe Schnaible[27], Richard P. Schwarz[67], Ramatholo Sefako[68], Aleksandra Selezneva[46],
Brett Skinner[27], Chris Stockdale[69], Ivan A. Strakhov[15], Thiam-Guan Tan[70], Guillermo Torres[6], René Tronsgaard[30],
Joseph D. Twicken[3,5], David Vermilion[4,37], Ian A. Waite[71], Bradley Walter[35,72,73], Gavin Wang[74], Carl Ziegler[75], and
Yujie Zou[51]

[1] Department of Astronomy, University of California Berkeley, Berkeley, CA 94720, USA; steven_giacalone@berkeley.edu
[2] Bay Area Environmental Research Institute, P.O. Box 25, Moffett Field, CA 94035, USA
[3] NASA Ames Research Center, Moffett Field, CA 94035, USA
[4] NASA Goddard Space Flight Center, 8800 Greenbelt Road, Greenbelt, MD 20771, USA
[5] SETI Institute, 189 Bernardo Avenue, Suite 200, Mountain View, CA 94043, USA
[6] Center for Astrophysics | Harvard & Smithsonian, 60 Garden Street, Cambridge, MA 02138, USA
[7] Department of Physics & Astronomy, Swarthmore College, Swarthmore PA 19081, USA
[8] Department of Astronomy, Columbia University, 550 W 120th Street, New York, NY 10027, USA
[9] NASA Exoplanet Science Institute, Caltech/IPAC, Mail Code 100-22, 1200 E. California Boulevard, Pasadena, CA 91125, USA
[10] Departmento de Astrofísica, Centro de Astrobiología (CAB, CSIC-INTA), Depto. de Astrofísica, ESAC campus, E-28692 Villanueva de la Cañada (Madrid), Spain
[11] Astrobiology Research Unit, Université de Liège, 19C Allée du 6 Août, B-4000 Liège, Belgium
[12] Department of Earth, Atmospheric and Planetary Science, Massachusetts Institute of Technology, 77 Massachusetts Avenue, Cambridge, MA 02139, USA
[13] Observatoire de l'Université de Genève, Chemin Pegasi 51, 1290 Versoix, Switzerland
[14] Department of Astronomy, University of Tokyo, 7-3-1 Hongo, Bunkyo-ku, Tokyo 113-0033, Japan
[15] Sternberg Astronomical Institute, M.V. Lomonosov Moscow State University, 13, Universitetskij pr., 119234, Moscow, Russia
[16] Institute for Research on Exoplanets (IREx), Université de Montréal, Département de Physique, C.P. 6128 Succ. Centre-ville, Montréal, QC H3C 3J7, Canada
[17] Department of Physics and Astronomy, University of Kansas, Lawrence, KS, USA
[18] Department of Astronomy and Astrophysics, University of Chicago, 5640 S. Ellis Avenue, Chicago, IL 60637, USA
[19] University of Maryland, Baltimore County, 1000 Hilltop Circle, Baltimore, MD 21250, USA
[20] The Adler Planetarium, 1300 South Lakeshore Drive, Chicago, IL 60605, USA
[21] GSFC Sellers Exoplanet Environments Collaboration, USA
[22] Department of Physics and Kavli Institute for Astrophysics and Space Research, Massachusetts Institute of Technology, Cambridge, MA 02139, USA
[23] Department of Earth, Atmospheric and Planetary Sciences, Massachusetts Institute of Technology, Cambridge, MA 02139, USA
[24] Department of Aeronautics and Astronautics, Massachusetts Institute of Technology, 77 Massachusetts Avenue, Cambridge, MA 02139, USA
[25] Department of Astrophysical Sciences, Princeton University, Peyton Hall, 4 Ivy Lane, Princeton, NJ 08540, USA
[26] Department of Physics & Astronomy, University of California Los Angeles, Los Angeles, CA 90095, USA
[27] Physics Department, Austin College, Sherman, TX 75090, USA
[28] Department of Astronomy and Astrophysics, University of California, Santa Cruz, CA 95060, USA
[29] Oukaimeden Observatory, High Energy Physics and Astrophysics Laboratory, Cadi Ayyad University, Marrakech, Morocco
[30] DTU Space, National Space Institute, Technical University of Denmark, Elektrovej 328, DK-2800 Kgs. Lyngby, Denmark
[31] Dipartimento di Fisica E. Pancini, Università di Napoli Federico II, Via Cinthia I-80126, Napoli, Italy
[32] European Southern Observatory, Karl-Schwarzschild-Strasse 2 D-85748 Garching bei Munchen, Germany
[33] Institute for Astronomy, University of Hawai'i, 2680 Woodlawn Drive, Honolulu, HI 96822, USA
[34] George Mason University, 4400 University Drive, Fairfax, VA 22030 USA
[35] American Association of Variable Star Observers, 49 Bay State Road, Cambridge, MA 02138, USA
[36] Boyce Research Initiatives and Education Foundation, San Diego, CA, USA
[37] Department of Physics and Astronomy, George Mason University, 4400 University Drive, Fairfax, VA 22030, USA
[38] University of Khartoum, Faculty of Science, Department of Physics, P.O.BOX 321, Khartoum, 11111, Sudan
[39] Instituto de Astrofísica de Canarias (IAC), E-38205 La Laguna, Tenerife, Spain
[40] Departamento de Astrofísica, Universidad de La Laguna (ULL), 38206, La Laguna, Tenerife, Spain
[41] Kavli Institute for Astrophysics and Space Research, Massachusetts Institute of Technology, Cambridge, MA 02139, USA
[42] Komaba Institute for Science, The University of Tokyo, 3-8-1 Komaba, Meguro, Tokyo 153-8902, Japan
[43] Department of Astronomy and Tsinghua Centre for Astrophysics, Tsinghua University, Beijing 100084, People's Republic of China

[44] Grand Pra Observatory, 1984 Les Hauderes, Switzerland
[45] University of California, Santa Cruz, 1156 High Street, Santa Cruz, CA 95064, USA
[46] Observatori Astronòmic Albanyà, Camí de Bassegoda S/N, Albanyà E-17733, Girona, Spain
[47] Department of Physics, Southern Connecticut State University, 501 Crescent Street, New Haven, CT 06515, USA
[48] Nicolaus Copernicus Astronomical Center of the Polish Academy of Sciences, ul. Rabiańska 8, 87-100, Toruń, Poland
[49] Department of Astronomy, California Institute of Technology, Pasadena, CA 91125, USA
[50] Campo Catino Astronomical Observatory, Regione Lazio, Guarcino (FR), I-03010 Italy
[51] Department of Multi-Disciplinary Sciences, Graduate School of Arts and Sciences, The University of Tokyo, 3-8-1 Komaba, Meguro, Tokyo 153-8902, Japan
[52] Department of Earth and Planetary Sciences, University of California, Riverside, CA 92521, USA
[53] Department of Physics and Astronomy, University of Louisville, Louisville, KY 40292, USA
[54] The Maury Lewin Astronomical Observatory, Glendora, CA 91741. USA
[55] National Astronomical Observatories, Chinese Academy of Sciences, 20A Datun Road, Chaoyang District, Beijing 100012, People's Republic of China
[56] Villa '39 Observatory, Landers, CA 92285, USA
[57] U.S. Naval Observatory, 3450 Massachusetts Avenue NW, Washington, D.C. 20392, USA
[58] Department of Physics and Astronomy, University of New Mexico, 210 Yale Blvd NE, Albuquerque, NM 87106, USA
[59] Department of Astronomy, Graduate School of Science, The University of Tokyo, 7-3-1 Hongo, Bunkyo-ku, Tokyo 113-0033, Japan
[60] Astrobiology Center, 2-21-1 Osawa, Mitaka, Tokyo 181-8588, Japan
[61] Space Sciences, Technologies and Astrophysics Research (STAR) Institute, Université de Liège, 19C Allée du 6 Août, B-4000 Liège, Belgium
[62] Department of Physics & Astronomy, University of California Irvine, Irvine, CA 92697, USA
[63] Royal Astronomical Society, Burlington House, Piccadilly, London W1J 0BQ, UK
[64] Space Telescope Science Institute, 3700 San Martin Drive, Baltimore, MD 21218, USA
[65] Department of Physics and Astronomy, Johns Hopkins University, 3400 N Charles Street, Baltimore, MD 21218, USA
[66] Department of Astronomy, University of Maryland, College Park, College Park, MD 20742 USA
[67] Patashnick Voorheesville Observatory, Voorheesville, NY 12186, USA
[68] South African Astronomical Observatory, P.O. Box 9, Observatory, Cape Town 7935, South Africa
[69] Hazelwood Observatory, Australia
[70] Perth Exoplanet Survey Telescope, Perth, Western Australia
[71] Centre for Astrophysics, University of Southern Queensland, Toowoomba, QLD, 4350, Australia
[72] Central Texas Astronomical Society, 8301 Bosque Boulevard, Waco, TX 76712, USA
[73] McMahan Observatory, 11056 FM 86, Lockhart, TX 78644, USA
[74] Tsinghua International School, Beijing 100084, People's Republic of China
[75] Department of Physics, Engineering and Astronomy, Stephen F. Austin State University, 1936 North Street, Nacogdoches, TX 75962, USA

Abstract

The James Webb Space Telescope will be able to probe the atmospheres and surface properties of hot, terrestrial planets via emission spectroscopy. We identify 18 potentially terrestrial planet candidates detected by the Transiting Exoplanet Survey Satellite (TESS) that would make ideal targets for these observations. These planet candidates cover a broad range of planet radii ($R_p \sim 0.6$–$2.0 R_\oplus$) and orbit stars of various magnitudes ($K_s = 5.78$–10.78, $V = 8.4$–15.69) and effective temperatures ($T_{eff} \sim 3000$–6000 K). We use ground-based observations collected through the TESS Follow-up Observing Program (TFOP) and two vetting tools—DAVE and TRICERATOPS—to assess the reliabilities of these candidates as planets. We validate 13 planets: TOI-206 b, TOI-500 b, TOI-544 b, TOI-833 b, TOI-1075 b, TOI-1411 b, TOI-1442 b, TOI-1693 b, TOI-1860 b, TOI-2260 b, TOI-2411 b, TOI-2427 b, and TOI-2445 b. Seven of these planets (TOI-206 b, TOI-500 b, TOI-1075 b, TOI-1442 b, TOI-2260 b, TOI-2411 b, and TOI-2445 b) are ultra-short-period planets. TOI-1860 is the youngest (133 ± 26 Myr) solar twin with a known planet to date. TOI-2260 is a young (321 ± 96 Myr) G dwarf that is among the most metal-rich ([Fe/H] = 0.22 ± 0.06 dex) stars to host an ultra-short-period planet. With an estimated equilibrium temperature of ~ 2600 K, TOI-2260 b is also the fourth hottest known planet with $R_p < 2 R_\oplus$.

Unified Astronomy Thesaurus concepts: Exoplanet astronomy (486); Exoplanet atmospheres (487); Exoplanet systems (484); Exoplanets (498); Exoplanet surfaces (2118); Exoplanet evolution (491); Transit photometry (1709)

1. Introduction

Over the last two decades, the combination of planet radii (R_p) and planet masses (M_p) measured from transit and radial velocity (RV) observations have enabled the calculations of bulk densities for hundreds of exoplanets. With the help of theoretical models of the interior structures of planets (Valencia et al. 2006, 2007a, 2007b; Fortney et al. 2007; Seager et al. 2007;

Zeng & Seager 2008; Grasset et al. 2009; Zeng & Sasselov 2013; Zeng et al. 2016), the bulk densities of these planets have made it possible to identify planets with terrestrial compositions (e.g., Batalha et al. 2011; Carter et al. 2012; Dragomir et al. 2013; Barros et al. 2014; Dressing et al. 2015; Rogers 2015; Motalebi et al. 2015; Gillon et al. 2017b). As a consequence, our understanding of terrestrial planets outside of the solar system has progressed significantly in recent years. For instance, terrestrial planets with orbital periods shorter than 30 days are now known to have maximum radii between 1.5 and 2.0 $R_\oplus$ (e.g., Rogers 2015; Buchhave et al. 2016).

Another notable discovery resulting from these surveys is the distinct gap in occurrence rate between planets with $R_p < 1.5 R_\oplus$ and planets with $R_p > 2.0 R_\oplus$ (Fulton et al. 2017; Fulton & Petigura 2018; often referred to as the "radius gap"), with the former regime corresponding to planets with terrestrial

compositions and the latter regime corresponding to planets with volatile-rich gaseous envelopes. This feature has important implications for the formation and evolution of short-period terrestrial planets, and several theories have predicted it or put forth an explanation for its origin. Some have proposed that the gap is a natural consequence of planets forming in gas-poor and gas-rich environments (Lee et al. 2014; Lee & Chiang 2016; Lopez & Rice 2018), while others contend that the gap is a result of atmospheric loss via photoevaporation (Jackson et al. 2012; Lopez & Fortney 2013; Owen & Wu 2013; Jin et al. 2014; Owen & Wu 2017; Jin & Mordasini 2018), core-powered mass loss (Ginzburg et al. 2016, 2018), or planetesimal collision (Shuvalov 2009; Schlichting et al. 2015). This gap has also been found to depend on planet orbital period (Van Eylen et al. 2018; Martinez et al. 2019), stellar mass (Fulton & Petigura 2018; Wu 2019; Cloutier & Menou 2020), and system age (Berger et al. 2020; David et al. 2020), which indicates that the terrestrial planet formation mechanism responsible for the feature could vary from system to system.

More recently, attempts have been made to more closely characterize terrestrial planets by observing their thermal emission phase curves. These near- and mid-infrared observations can reveal whether a terrestrial planet is surrounded by a thin atmosphere or has an airless surface, as only the former is expected to produce phase curves with evidence of atmospheric heat redistribution (Seager & Deming 2009; Selsis et al. 2011; Koll & Abbot 2016; Kreidberg & Loeb 2016). Using this method, Demory et al. (2016) found evidence of atmospheric circulation for 55 Cnc e, and Kreidberg et al. (2019) inferred the absence of an atmosphere for LHS 3844 b. In addition, Kreidberg et al. (2019) were able to use the wavelength-dependent planet-to-star flux ratio to estimate the surface composition of LHS 3844 b, finding that it is consistent with a basaltic composition that could result from widespread volcanism.

Our ability to characterize short-period terrestrial planets will improve drastically with the launch of the James Webb Space Telescope (JWST), which will allow for the characterization of exoplanet atmospheres and surface properties via transmission spectroscopy, emission spectroscopy, and emission photometry (Greene et al. 2016). For most of the known terrestrial planets, detecting atmospheric absorption features in transmission spectra would be extremely challenging (the exception being those orbiting ultracool dwarfs and white dwarfs; Lustig-Yaeger et al. 2019; Kaltenegger et al. 2020), but many of these planets would make excellent targets for thermal emission measurements. With these observations, one can infer the presence or lack of atmospheres surrounding short-period terrestrial planets (Koll et al. 2019; Lustig-Yaeger et al. 2019; Mansfield et al. 2019). For planets with atmospheres, relatively low-signal-to-noise-ratio (S/N) emission photometry and/or spectroscopy will reveal modest information about atmospheric composition and identify suitable targets for further atmospheric characterization with future high-precision instruments. For planets without atmospheres, emission measurements will permit the characterization of the surfaces of planets, such as those hot enough for the existence of dayside lava oceans (Rouan et al. 2011; Samuel et al. 2014; Kite et al. 2016; Essack et al. 2020).

The most highly anticipated JWST instrument for these observations is the Mid-Infrared Instrument (MIRI), which can perform low-resolution spectroscopy between 5 and 12 μm. This wavelength range contains a number of features that can be used to discern planets with atmospheres from those without atmospheres. Morley et al. (2017) and Lincowski et al. (2018) simulated emission spectra for several terrestrial exoplanets assuming various atmospheric compositions, finding a number of notable absorption features. Specifically, Earth-like and O_2-dominated outgassed atmospheres can be identified via strong H_2O absorption between 5 and 7 μm, whereas Venus-like atmospheres display prominent SO_2 absorption between 7 and 9 μm and strong CO_2 absorption above 10 μm. Lincowski et al. (2018) also modeled the case of O_2-dominated desiccated (water-poor) atmospheres, which may be particularly relevant for planets orbiting M dwarfs (Luger & Barnes 2015), finding that they are distinguishable by a lack of H_2O absorption between 5 and 7 μm and strong O_3 absorption at 9.6 μm. Zilinskas et al. (2020) modeled emission spectra of N_2-dominated atmospheres for the hot terrestrial planet 55 Cnc e, finding that C-rich atmospheres have a distinct HCN feature at 7.5 μm. Hu et al. (2012) considered the cases of hot planets with airless surfaces when simulating thermal emission spectra. These spectra are largely blackbody-like but feature notable SiO absorption between 7 and 13 μm, which could be abundant for planets close enough to their host stars for their surfaces to vaporize (Schaefer et al. 2012). This SiO absorption is expected to vary based on the types of rocks being vaporized (e.g., basaltic versus feldspathic versus ultramafic) and can therefore reveal information about surface composition.

In anticipation of the launch of JWST, many have designed methods and frameworks for identifying good targets for thermal emission observations (e.g., Batalha et al. 2017; Kempton et al. 2018). Kempton et al. (2018) defined the emission spectroscopy metric (ESM), a proxy for the S/N attainable for a terrestrial planet being observed with emission spectroscopy, in order to determine what planets should be prioritized for these observations, drawing the threshold above which the best targets exist at 7.5. As of 2018, only seven confirmed terrestrial planets (GJ 1132 b, HD 219134 b, HD 219134 c, 55 Cnc e, HD 3167 b, K2-141 b, and GJ 9827 b) had met this criterion, and three of these (HD 219134 b, HD 219134 c, and 55 Cnc e) have host stars too bright for emission spectroscopy observations with JWST. If an extensive emission photometry/spectroscopy survey of short-period terrestrial planets is to be conducted, more of these planets must be discovered.

The Transiting Exoplanet Survey Satellite mission (TESS; Ricker et al. 2010), an ongoing survey searching for transiting planets across nearly the entire sky, has already significantly expanded the size of this sample. Since the start of the mission in mid-2018, an additional 15 planets with $R_p < 2 R_\oplus$, ESM > 7.5, and host stars amenable to JWST observations have been discovered. In addition, we have identified 18 TESS Objects of Interest (TOIs; Guerrero et al. 2021), stars that exhibit decreases in brightness consistent with the signals caused by transiting planets, that would also meet these requirements if confirmed to host planets with terrestrial compositions. Nonetheless, because some of these TOIs could end up being astrophysical false positives (FPs; such as eclipsing binaries around nearby stars contaminating the TESS aperture), the community would benefit from a vetting analysis that identifies the potentially terrestrial planet candidates that have the best chances of being bona fide planets. In this paper, we scrutinize TESS data and follow-up observations to assess

Table 1
TOI Parameters from TICv8.1 and ExoFOP

TOI	K_s mag	Parallax (mas)	$T_{\rm eff}$ (K)	$\log g$	$R_\star$ ($R_\odot$)	δ (ppm)	$R_{\rm p}$ ($R_\oplus$)	$P_{\rm orb}$ (days)	ESM
206.01	10.06 ± 0.02	20.92 ± 0.05	3380 ± 160	4.87 ± 0.01	0.35 ± 0.01	1540 ± 230	1.51 ± 0.12	0.736	8.7 ± 1.4
500.01	7.73 ± 0.03	21.07 ± 0.02	4450 ± 130	4.53 ± 0.10	0.75 ± 0.06	246 ± 27	1.29 ± 0.13	0.548	9.3 ± 1.2
539.01	9.23 ± 0.02	9.20 ± 0.02	4900 ± 130	4.52 ± 0.09	0.81 ± 0.05	310 ± 40	1.56 ± 0.14	0.310	8.1 ± 1.1
544.01	7.80 ± 0.02	24.29 ± 0.04	4220 ± 120	4.61 ± 0.11	0.66 ± 0.06	590 ± 6	1.76 ± 0.16	1.549	10.3 ± 0.9
731.01	5.78 ± 0.02	106.21 ± 0.03	3540 ± 160	4.78 ± 0.01	0.46 ± 0.01	242 ± 20	0.78 ± 0.04	0.322	20.4 ± 1.7
833.01	8.15 ± 0.03	23.94 ± 0.02	3920 ± 160	4.65 ± 0.01	0.60 ± 0.02	580 ± 60	1.58 ± 0.10	1.042	10.0 ± 1.2
1075.01	9.11 ± 0.02	16.24 ± 0.03	3920 ± 160	4.67 ± 0.01	0.58 ± 0.02	970 ± 90	1.97 ± 0.10	0.605	14.7 ± 1.3
1242.01	9.77 ± 0.03	9.06 ± 0.03	4250 ± 130	4.56 ± 0.11	0.71 ± 0.07	578 ± 32	1.87 ± 0.18	0.381	9.8 ± 0.9
1263.01	7.10 ± 0.02	21.45 ± 0.04	5100 ± 130	4.55 ± 0.08	0.82 ± 0.05	258 ± 32	1.43 ± 0.12	1.021	9.9 ± 1.3
1411.01	7.25 ± 0.02	30.76 ± 0.02	4180 ± 120	4.57 ± 0.11	0.69 ± 0.06	366 ± 21	1.44 ± 0.14	1.452	8.9 ± 0.9
1442.01	10.09 ± 0.02	24.26 ± 0.04	3330 ± 160	4.92 ± 0.01	0.31 ± 0.01	1350 ± 80	1.24 ± 0.05	0.409	10.3 ± 0.7
1693.01	8.33 ± 0.02	32.44 ± 0.04	3470 ± 160	4.77 ± 0.01	0.46 ± 0.01	1010 ± 120	1.60 ± 0.11	1.767	7.8 ± 1.1
1860.01	6.79 ± 0.02	21.78 ± 0.03	5670 ± 100	4.51 ± 0.07	0.93 ± 0.04	232 ± 29	1.54 ± 0.12	1.066	11.1 ± 1.5
2260.01	8.68 ± 0.02	9.85 ± 0.03	5430 ± 130	4.51 ± 0.08	0.90 ± 0.05	313 ± 35	1.73 ± 0.13	0.352	10.5 ± 1.3
2290.01	9.07 ± 0.02	17.19 ± 0.02	3860 ± 160	4.68 ± 0.01	0.57 ± 0.02	600 ± 60	1.51 ± 0.09	0.386	11.8 ± 1.2
2411.01	8.53 ± 0.02	16.77 ± 0.08	4100 ± 120	4.52 ± 0.11	0.73 ± 0.07	520 ± 50	1.81 ± 0.19	0.783	10.7 ± 1.4
2427.01	7.05 ± 0.02	35.04 ± 0.03	4070 ± 120	4.58 ± 0.11	0.68 ± 0.06	560 ± 24	1.75 ± 0.17	1.306	15.6 ± 1.6
2445.01	10.78 ± 0.02	20.56 ± 0.10	3330 ± 160	4.96 ± 0.01	0.27 ± 0.01	2400 ± 400	1.44 ± 0.12	0.371	13.0 ± 2.0

the possibility that these 18 TOIs are actual planets and argue for future characterization efforts.

In Section 2, we discuss our sample of 18 TOIs and describe how they were selected. In Section 3, we describe our vetting analysis procedure. In Section 4, we present follow-up observations of these TOIs that are incorporated into our analysis. In Section 5, we present the results of our vetting analysis and validate 13 of the TOIs. In Section 6, we discuss the implications of our results with respect to JWST emission spectroscopy. Lastly, in Section 7, we provide concluding remarks.

2. Sample

The goal of this paper is to identify a sample of small, hot, and likely terrestrial planets that would be favorable targets for emission spectroscopy observations with JWST. We select our sample by first identifying all TOIs with orbital periods ($P_{\rm orb}$) < 10 days and $R_{\rm p} < 2\,R_\oplus$, which corresponds approximately to the largest a planet can be without having a volatile-rich gaseous envelope (e.g., Rogers 2015; Buchhave et al. 2016). The $P_{\rm orb}$ of each TOI is gathered from ExoFOP-TESS.[79] We estimate the $R_{\rm p}$ of each TOI using the transit depths (δ) listed on ExoFOP-TESS and the stellar properties in version 8.1 of the TESS Input Catalog (TIC; Stassun et al. 2018).[80] Next, we remove all TOIs that have been flagged as FPs or false alarms (FAs) on ExoFOP-TESS under "TFOPWG Disposition." FPs are typically caused by eclipsing binaries around stars close enough to the target star to contaminate the TESS aperture, while FAs are typically caused by stellar rotation or instrumental variability that produces a signal resembling a planetary transit. Because the events caused by FPs and FAs are often shallow enough to be mistaken as the transits of small planets, scrutinizing observations of small TOIs for FP and FA signatures is an important step in determining which are bona fide planets. Our procedure for further vetting TOIs that pass this condition is described in Section 3.

Lastly, we determine which of our planet candidates would be most amenable to thermal emission measurements with JWST. To do this, we calculate the emission spectroscopy metric (ESM) for each of the remaining TOIs. The ESM is a quantity introduced in Kempton et al. (2018) to serve as a proxy for the S/N one should expect to obtain when observing the emission spectrum of an exoplanet with JWST. More specifically, ESM is given by the equation

$$\text{ESM} = 4.26 \times 10^6 \times \frac{B_{7.5}(T_{\rm day})}{B_{7.5}(T_{\rm eff})} \times \left(\frac{R_{\rm p}}{R_\star}\right)^2 \times 10^{-m_K/5}, \quad (1)$$

where $B_{7.5}$ is Planck's function evaluated at 7.5 μm for a given temperature, $T_{\rm day}$ is the dayside temperature of the planet in Kelvin (which is assumed to be 1.1× the equilibrium temperature of the planet), $T_{\rm eff}$ is the effective temperature of the host star in Kelvin, $R_\star$ is the stellar radius, and m_K is the apparent magnitude of the host star in the K band. When calculating equilibrium temperature (here and throughout the remainder of the paper), we assume zero bond albedo and full day–night heat redistribution.[81] Kempton et al. (2018) recommend that terrestrial planets with ESM $\gtrsim 7.5$ be prioritized for emission spectroscopy observations. We therefore remove TOIs with ESMs lower than this threshold. The host star and the planet properties of our final list of 18 TOIs are shown in Table 1.

It is worth noting that small planets are not the only good targets for JWST emission spectroscopy. In fact, Equation (1) shows that larger planets with thick atmospheres would produce an even higher signal through these observations. However, this paper focuses specifically on terrestrial planets.

2.1. Light-curve Generation

All of our TOIs were identified by the NASA Science Processing Operations Center (SPOC) pipeline (Jenkins et al. 2016), which analyzes data collected at a 2 minute or 20 s cadence. The SPOC pipeline identifies potential TOIs by

---

[79] https://exofop.ipac.caltech.edu/tess/index.php—search performed on 2021 March 11.
[80] $P_{\rm orb}$ and δ are reported by the SPOC pipeline, which is discussed further below.

[81] We acknowledge that, due to these assumptions, all equilibrium temperatures discussed in this paper are only rough estimates.

conducting a search for transiting planet signatures using a wavelet-based, adaptive noise-compensating matched filter with the Transiting Planet Search (TPS; Jenkins 2002; Jenkins et al. 2010) algorithm. It then performs a limb-darkened transit model fit to the detected signatures (Li et al. 2019) and constructs a number of diagnostic tests to help assess the planetary nature of the detected signals (Twicken et al. 2018), which are compiled in data validation reports. The pipeline then removes the transits of each potential signature and calls TPS to detect additional transiting planet signatures, stopping when it fails to identify additional transits or reaches a limit of eight detected signatures. The SPOC pipeline generates two light curves for each TOI: light curves extracted via simple aperture photometry (SAP; Twicken et al. 2010; Morris et al. 2020), and light curves extracted via SAP with an additional presearch data conditioning step (PDCSAP; Stumpe et al. 2012; Smith et al. 2012; Stumpe et al. 2014). The PDC step aids in planet detection by removing background trends and flux contamination due to nearby bright stars, a process that is well established in exoplanet transit surveys (Stumpe et al. 2012).

While the SPOC pipeline typically generates light curves that are sufficient for analyzing transits, it is not designed to preserve out-of-transit variation originating from the system. Because we are interested in whether our planet candidates show evidence of phase curves caused by reflected light in the TESS data, we take a different approach to extracting light curves that detrends the instrument systematics and stellar rotation signal while preserving transits and potential secondary eclipses. First, using the same approach as that discussed in Hedges et al. (2021), we build design matrices consisting of (1) an estimate of the TESS scattered light background based on the top four principal components of the pixels outside of the optimum pipeline aperture, estimated via singular value decomposition, (2) a basis spline with a knot spacing of 0.25 days to capture stellar variability, (3) the centroids of the image in column and row dimension, (4) the single-scale cotrending basis vectors (CBVs) from the TESS pipeline, (5) a simple BLS transit model, at a fixed period, transit midpoint, and duration, and (6) a simple eclipse model, consisting of a cosine phase curve and a simple box eclipse at phase 0.5. Using the same methods from Hedges et al. (2020), we fit these design matrices to all sectors simultaneously, fitting a single transit and a single-eclipse model for all sectors but allowing each individual sector to have unique solutions for the background, spline, centroid, and CBV matrices. By taking this approach of fitting all the sectors simultaneously, we are the most sensitive to the small signal of eclipses, because all sectors are able to contribute to our eclipse measurement. Even with this rigorous approach, we detect no eclipse with a $\geqslant 3\sigma$ significance for the planet candidates in this paper.

Our light-curve generation code does not subtract out contamination due to nearby stars, which is an important step for correctly determining the radius of a planet candidate. However, because the code uses the same apertures as the SPOC pipeline, we are able to remove contamination using the crowding factor (labeled as CROWDSAP in the PDCSAP FITS headers) for each of our targets. We perform this subtraction when fitting the photometry for the orbital and physical parameters of the planet candidates, which is further described in Section 2.3.

Table 2
Adopted Stellar Parameters

TOI	$T_{\rm eff}$ (K)	$\log g$	$M_{\star}$ ($M_{\odot}$)	$R_{\star}$ ($R_{\odot}$)
206	3383 ± 157	4.89 ± 0.03	0.35 ± 0.01	0.35 ± 0.01
500	4621 ± 50	4.63 ± 0.10	0.88 ± 0.25	0.75 ± 0.06
539	5031 ± 50	4.58 ± 0.10	0.91 ± 0.24	0.81 ± 0.05
544	4369 ± 100	4.73 ± 0.10	0.85 ± 0.20	0.66 ± 0.02
731	3540 ± 160	4.79 ± 0.03	0.48 ± 0.03	0.46 ± 0.01
833	3920 ± 160	4.67 ± 0.04	0.61 ± 0.03	0.60 ± 0.02
1075	3921 ± 157	4.69 ± 0.03	0.60 ± 0.02	0.58 ± 0.02
1242	4348 ± 100	4.69 ± 0.10	0.83 ± 0.31	0.68 ± 0.10
1263	5166 ± 50	4.54 ± 0.10	0.78 ± 0.20	0.82 ± 0.05
1411	4266 ± 100	4.73 ± 0.10	0.59 ± 0.23	0.66 ± 0.10
1442	3330 ± 160	4.92 ± 0.04	0.29 ± 0.02	0.31 ± 0.01
1693	3499 ± 70	4.80 ± 0.03	0.49 ± 0.03	0.46 ± 0.01
1860	5752 ± 100	4.58 ± 0.10	0.99 ± 0.03	0.94 ± 0.02
2260	5534 ± 100	4.62 ± 0.10	0.99 ± 0.04	0.94 ± 0.05
2290	3813 ± 70	4.70 ± 0.02	0.56 ± 0.01	0.57 ± 0.02
2411	4099 ± 123	4.59 ± 0.03	0.65 ± 0.02	0.68 ± 0.02
2427	4072 ± 121	4.62 ± 0.03	0.64 ± 0.02	0.65 ± 0.02
2445	3333 ± 157	4.97 ± 0.04	0.25 ± 0.01	0.27 ± 0.01

2.2. Adopted Stellar Parameters

We adopt stellar parameters for each of our host stars using a combination of spectrum analysis and empirical relation. The tools used to calculate stellar parameters from spectra are outlined in Section 4.2, and the empirical relations used to calculate stellar parameters are described below. Because different methods yield different parameters (e.g., some spectrum-based analysis methods only provide effective temperature and surface gravity, whereas others also provide estimates for stellar mass and radius), we take a curated approach for each of our stars. We describe this process in detail here and present the adopted parameters in Table 2.

When available, we use spectra to estimate $T_{\rm eff}$. Where more than one spectrum-based estimate of $T_{\rm eff}$ is available, we adopt the average of the estimates. If spectra are not available, or if our stellar classification tools are unable to estimate parameters for a given star (which is sometimes the case for stars with $T_{\rm eff} \leqslant 4500$ K), we adopt the $T_{\rm eff}$ listed in the TIC.

For stars observed with Keck/HIRES and $T_{\rm eff} > 4250$ K, we adopt the $R_{\star}$ estimated from the spectrum. For all other stars with $T_{\rm eff} > 4250$ K, we adopt the $R_{\star}$ listed in the TIC. For all stars with $T_{\rm eff} \leqslant 4250$ K, we estimate $R_{\star}$ and its uncertainties with the calibrations by Mann et al. (2015), using the 2MASS $K_{\rm S}$-band magnitudes and Gaia/DR2 parallaxes.

For stars observed with Keck/HIRES and $T_{\rm eff} > 4700$ K, we adopt the stellar mass ($M_{\star}$) estimated from the spectrum. For all other stars with observed spectra and $T_{\rm eff} > 4250$ K, we calculate $M_{\star}$ using the $R_{\star}$ listed in the TIC and the surface gravity estimated from the spectra. For all stars with $T_{\rm eff} \leqslant 4250$ K, we estimate $M_{\star}$ with the near-infrared mass–luminosity calibrations in Mann et al. (2019) and Benedict et al. (2016; adopting the average of the two), using the 2MASS $K_{\rm S}$-band magnitudes and Gaia/DR2 parallaxes.

For stars with observed spectra and $T_{\rm eff} > 4250$ K, we adopt the surface gravity ($\log g$) estimated from the spectra. Where more than one spectrum-based estimate of $\log g$ is available, we adopt the average of the estimates. For all other stars, $\log g$ is calculated using the values of $M_{\star}$ and $R_{\star}$ determined with the methods described above.

Table 3
Best-fit Planet Parameters

TOI	$R_{\rm p}$ ($R_\oplus$)	$P_{\rm orb}$ (days)	T_0 (BJD—2457000)	b	a (au)	$T_{\rm eq}$	ESM
206.01	1.30 ± 0.05	0.7363104 ± 0.0000003	1325.5431 ± 0.0004	0.66 ± 0.03	0.0112 ± 0.0001	910 ± 36	6.4 ± 0.5
500.01	1.16 ± 0.12	0.5481579 ± 0.0000006	1468.3917 ± 0.0006	0.58 ± 0.17	0.0128 ± 0.0011	1693 ± 105	7.3 ± 1.2
539.01	1.25 ± 0.10	0.3096071 ± 0.0000004	1354.1044 ± 0.0009	0.39 ± 0.20	0.0089 ± 0.0007	2311 ± 108	5.1 ± 0.6
544.01	2.03 ± 0.10	1.5483510 ± 0.0000015	1469.7570 ± 0.0005	0.64 ± 0.08	0.0251 ± 0.0019	1082 ± 47	13.0 ± 1.8
731.01	0.59 ± 0.02	0.3219659 ± 0.0000004	1543.4874 ± 0.0006	0.09 ± 0.07	0.0069 ± 0.0001	1416 ± 65	11.5 ± 0.6
833.01	1.27 ± 0.07	1.0418777 ± 0.0000324	1597.2560 ± 0.0010	0.31 ± 0.14	0.0171 ± 0.0003	1118 ± 49	6.5 ± 0.6
1075.01	1.72 ± 0.08	0.6047328 ± 0.0000032	1654.2511 ± 0.0008	0.18 ± 0.12	0.0118 ± 0.0001	1336 ± 56	10.9 ± 1.0
1242.01	1.65 ± 0.23	0.3814851 ± 0.0000004	1683.7103 ± 0.0004	0.40 ± 0.22	0.0097 ± 0.0010	1751 ± 110	7.7 ± 1.4
1263.01	1.36 ± 0.11	1.0213646 ± 0.0001277	1683.5569 ± 0.0018	0.37 ± 0.19	0.0185 ± 0.0014	1656 ± 75	9.2 ± 1.3
1411.01	1.36 ± 0.16	1.4520358 ± 0.0000098	1739.4762 ± 0.0014	0.32 ± 0.20	0.0230 ± 0.0026	1136 ± 59	7.6 ± 1.1
1442.01	1.17 ± 0.06	0.4090677 ± 0.0000003	1683.4523 ± 0.0003	0.33 ± 0.13	0.0071 ± 0.0002	1072 ± 54	8.9 ± 0.8
1693.01	1.41 ± 0.10	1.7666957 ± 0.0000054	1817.6827 ± 0.0014	0.30 ± 0.14	0.0226 ± 0.0004	764 ± 19	6.0 ± 0.9
1860.01	1.31 ± 0.04	1.0662107 ± 0.0000014	1683.6041 ± 0.0003	0.69 ± 0.02	0.0204 ± 0.0002	1885 ± 28	7.9 ± 0.4
2260.01	1.62 ± 0.13	0.3524728 ± 0.0000047	1928.2390 ± 0.0007	0.77 ± 0.04	0.0097 ± 0.0001	2609 ± 86	8.7 ± 0.9
2290.01	1.17 ± 0.07	0.3862224 ± 0.0000033	1764.9871 ± 0.0013	0.27 ± 0.15	0.0086 ± 0.0001	1484 ± 31	7.1 ± 0.8
2411.01	1.68 ± 0.11	0.7826942 ± 0.0000037	2116.0139 ± 0.0010	0.39 ± 0.14	0.0144 ± 0.0001	1355 ± 45	9.9 ± 1.2
2427.01	1.80 ± 0.12	1.3060011 ± 0.0000102	2169.6202 ± 0.0004	0.87 ± 0.02	0.0202 ± 0.0002	1117 ± 46	17.2 ± 2.1
2445.01	1.25 ± 0.08	0.3711281 ± 0.0000005	2144.5697 ± 0.0004	0.27 ± 0.14	0.0064 ± 0.0001	1060 ± 54	9.6 ± 1.2

2.3. Transit Fits

To estimate the orbital and planetary parameters for each of our planet candidates, we fit each of our light curves with Markov Chain Monte Carlo sampling using the exoplanet (Foreman-Mackey et al. 2021) Python package. Our transit model assumed a circular orbit and was initialized with the following priors: (1) Gaussian priors for $M_\star$ and $R_\star$, (2) a Gaussian prior for the natural logarithm of $P_{\rm orb}$, (3) a Gaussian prior for the time of inferior conjunction (T_0), (4) a uniform prior for the impact parameter (b), (5) uniform priors for quadratic limb-darkening coefficients (Kipping 2013), (6) a Gaussian prior for the natural logarithm of the transit depth, and (7) a Gaussian prior for the flux zero point of the light curve. For each TOI, we run a 10 walker ensemble for 20,000 steps and ensure that convergence was achieved, then discard the first 10,000 steps as burn-in. The best-fit parameters for each planet candidate are shown in Table 3, and the corresponding best-fit light-curve models are shown in Figure 1.

For most of the TOIs in this paper, these fits only include TESS data. However, transits of TOI-206.01, TOI-1075.01, TOI-1442.01, TOI-1693.01, TOI-2411.01, TOI-2411.01, TOI-2427.01, and TOI-2445.01 were also observed by ground-based telescopes. For these targets, we perform joint fits including both the TESS data and the ground-based data. We fit for limb-darkening coefficients, transit depth, and flux zero point independently for each data set while treating $M_\star$, $R_\star$, $P_{\rm orb}$, T_0, and b as parameters that are shared between the data sets. The ground-based data are discussed in Section 4.3. In these cases, we adopt the planet radii inferred from the TESS data.

Using these new planet properties, we recalculate the ESM for each TOI. All TOIs except for TOI-206.01, TOI-500.01, TOI-539.01, and TOI-1693.01 retained an ESM > 7.5. In addition, we find that TOI-544.01 may have a radius slightly larger than $2R_\oplus$. Even though these TOIs do not meet our initial selection criteria with their newly calculated properties, we keep them in our analysis.

3. Vetting Procedure

We examine each of the unconfirmed TOIs described in Table 1 using both follow-up observations and analyses with the vetting tools DAVE (Kostov et al. 2019) and TRICERA-TOPS (Giacalone & Dressing 2020; Giacalone et al. 2021). Follow-up observations are used to search for evidence of FPs outside of the TESS data, while DAVE and TRICERATOPS are used to search for FP signatures within the TESS data.

We utilize three forms of follow-up observations in our vetting analysis. First, we acquired high-resolution images, such as those obtainable with adaptive optics, to search for unresolved companions (either bound or chance aligned) near the target. These companions can dilute the TESS transit, leading to an underestimation in the planet radius, or can even be the sources of FPs if the companion hosts an eclipsing binary (Ciardi et al. 2015; Furlan et al. 2017; Hirsch et al. 2017; Teske et al. 2018). Second, we obtained reconnaissance spectra to search for evidence of spectroscopic binaries around the target stars. Evidence of a binary star in the form of single-line or double-line spectroscopic binaries could either indicate that the planet candidate itself is an eclipsing binary or that there is an unresolved star in the system causing us to underestimate the radius of the planet candidate. In addition, deriving stellar parameters from spectra allows us to reaffirm the photometrically derived parameters in the TIC, which is important for a correct calculation of the planet radius and equilibrium temperature. Third, we used ground-based facilities with higher spatial resolutions than TESS to obtain time-series photometry of the field of stars within 2.'5 from the target during the time of transit. Because it is possible for nearby stars to contaminate the TESS aperture, transits due to nearby eclipsing binary stars can be mistakable as transits due to planet-size objects around the target star. These scenarios can be ruled out by either observing the transit on the target star, free of any contamination from nearby stars, or ruling out eclipsing binaries around all nearby stars bright enough to cause an FP. These observations are further described in Section 4.

Next, we analyze each TOI with DAVE, which vets planet candidates at both the pixel and light-curve levels. At the pixel
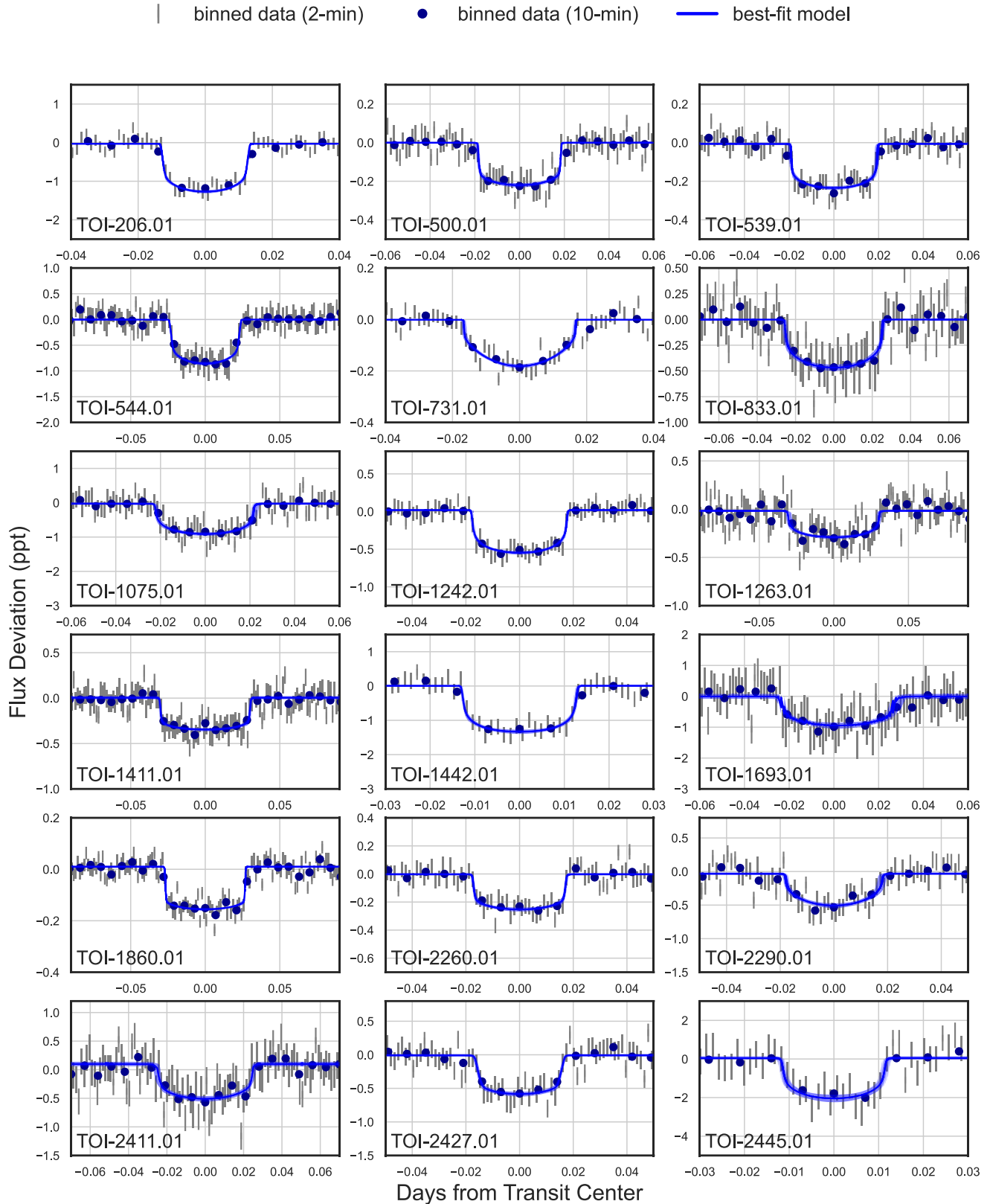
Figure 1. Phase-folded TESS data and best-fit transit models for each TOI. The parameters associated with these fits are shown in Table 3. The TESS data are purged of 5σ outliers and binned for clarity.

level, `DAVE` uses centroid offset analyses to identify evidence of FPs due to contamination from nearby stars. A similar difference image centroiding analysis is performed by the SPOC for each of its threshold-crossing events (TCEs; Twicken et al. 2018). For all TOIs, we cross-check with the corresponding SPOC data validation report to see if an offset is detected in the SPOC analysis. At the light-curve level, `DAVE` searches for signatures—such as differences in odd and even transits, secondary eclipses, and nontransit variability—that are indicative of FPs (e.g., Morton 2012; Ansdell et al. 2018; Shallue & Vanderburg 2018). For these analyses, we use the SAP/PDCSAP light curves generated by the SPOC pipeline.

Lastly, we analyze each TOI using `TRICERATOPS`, which vets a planet candidate by calculating the Bayesian probability that the candidate is an astrophysical FP. The analysis begins by querying the TIC for all stars in a $2.'5$ radius around the target star and modeling the TESS pixel response function to determine the amount of flux contamination each contributes to the aperture. For each star that contributes enough flux to cause the observed transit, the tool simulates light curves due to transiting planets and eclipsing binaries and calculates the marginal likelihood of each transit-producing scenario. These are combined with prior probabilities to calculate the FP probability (FPP; the total probability that the observed transit is due to something other than a transiting planet around the target star) and nearby FP probability (NFPP; the total probability that the observed transit originated from a known nearby star) for the planet candidate. A planet candidate that achieves a sufficiently small FPP (FPP < 0.01) and NFPP (NFPP < 10^{-3}) can be considered validated (Giacalone et al. 2021). For this analysis, we use the same light curves generated using the methodology described in Section 2.1 (without contamination due to nearby stars removed with the `CROWD-SAP` factor). Because the FPPs and NFPPs returned by `TRICERATOPS` have an intrinsic scatter, we run the tool 20 times on each TOI and report the means and standard deviations of these probabilities. Ultimately, we decide whether a planet is validated based on the results of this analysis.

`TRICERATOPS` also has the ability to fold in follow-up observations to place tighter constraints on the chances of FP scenarios. Specifically, high-resolution images are used to constrain the area of sky around the target where unresolved companion stars can exist. Folding in these data therefore reduces the probabilities of scenarios like those involving hierarchical and background eclipsing binaries. In addition, time-series photometry allows us to remove nearby stars that have been cleared from being eclipsing binaries from the analysis. When available, we utilize these data during this step of vetting.

4. Follow-up Observations

We analyze our TOIs using observations obtained by the TFOP Working Groups.[82] The data from these observations are available for download on the ExoFOP-TESS website and are summarized below.

4.1. High-resolution Imaging

We obtained high-resolution images of our TOIs using adaptive optics, speckle, and lucky imaging. In each of these

---

observations, we search for stars within $5''$ from the target star. In situations where companions were detected, we cross-checked the TIC to determine if these companions were previously known. These observations, which were obtained by members of TFOP Sub Group 3 (SG3), are summarized in Table 4, displayed in Figure 2, and discussed below.

4.1.1. CAHA/AstraLux

TOI-544, TOI-1238, TOI-1242, TOI-1411, TOI-1685, and TOI-2260 were observed with the high-spatial-resolution imaging instrument AstraLux (Hormuth et al. 2008) mounted on the 2.2 m telescope at Calar Alto Observatory (CAHA; Almería, Spain). The instrument uses the lucky-imaging technique (Fried 1978) by combining a fast readout and a small plate scale to obtain thousands of images with exposure times below the speckle coherence time and using the Sloan Digital Sky Survey z filter (SDSSz). We observed TOI-1411 on UT 2020 January 13, TOI-1242 on UT 2020 February 26, TOI-1238 and TOI-1685 on UT 2020 August 7, and TOI-544 and TOI-2260 on UT 2021 March 23. We used the following strategy for each target: 7000 frames of 10 ms exposure time to TOI-544, 126,500 frames of 20 ms for TOI-1238, 12,055 frames of 20 ms for TOI-1242, 98,600 frames of 10 ms for TOI-1411, 87,600 frames of 20 ms for TOI-1685, and 166,860 frames of 10 ms for TOI-2260. The number of frames and exposure time were adapted to achieve a magnitude contrast at $1''$ separation that would allow us to discard chance-aligned binaries mimicking the same transit depth as the planet candidates (see Lillo-Box et al. 2012, 2014). We choose a $6'' \times 6''$ field of view (FOV) in order to be able to reduce the individual exposure time down to the 10 ms level to improve the close-by sensitivity.

The data cubes were then reduced using the observatory pipeline (Hormuth et al. 2008). As a compromise between magnitude sensitivity and spatial resolution, we selected the 10% of the best frames according to their Strehl ratio (Strehl 1902) and then aligned and combined these images to compute a final high-spatial-resolution image per target. We computed the 5σ sensitivity curves for each of the images by using our own developed `astrasens` package[83] with the procedure described in Lillo-Box et al. (2014). We found no stellar companions within these computed sensitivity limits.

4.1.2. SAI/SPP

TOI-2260 and TOI-2290 were observed on UT 2021 February 2 and 2020 October 28, respectively, with the SPeckle Polarimeter (SPP; Safonov et al. 2017) on the 2.5 m telescope at the Caucasian Observatory of Sternberg Astronomical Institute (SAI) of Lomonosov Moscow State University. SPP uses an electron-multiplying CCD, Andor iXon 897, as a detector. The atmospheric dispersion compensator allowed for observations of these relatively faint targets through the wide-band I_c filter. Power spectra were estimated from 4000 frames with 30 ms exposures. The detector has a pixel scale of 20.6 mas pixel^{-1}. We did not detect any stellar companions in our observations. The 5σ sensitivity curves are presented in Figure 2.

Table 4
Summary of High-resolution Imaging Follow-up

TOI	Telescope	Instrument	Filter	Image Type	Companion (<5″)	Contrast (Δmag)				
						0″1	0″5	1″0	1″5	2″0
206	SOAR (4.1 m)	HRCam	I_c	Speckle	⋯	1.625	4.323	4.641	4.958	5.275
	Gemini-S (8 m)	Zorro	562 nm	Speckle	⋯	4.115	4.398	4.309	⋯	⋯
	Gemini-S (8 m)	Zorro	832 nm	Speckle	⋯	4.908	5.787	6.081	⋯	⋯
500	SOAR (4.1 m)	HRCam	I_c	Speckle	⋯	1.721	4.738	5.164	5.591	6.017
	Gemini-S (8 m)	Zorro	562 nm	Speckle	⋯	5.307	6.083	6.564	⋯	⋯
	Gemini-S (8 m)	Zorro	832 nm	Speckle	⋯	5.057	6.441	7.386	⋯	⋯
539	SOAR (4.1 m)	HRCam	I_c	Speckle	⋯	1.660	5.238	5.462	5.686	5.910
544	CAHA (2.2 m)	AstraLux	SDSSz	Lucky	⋯	2.614	6.015	4.053	⋯	⋯
	Shane (3 m)	ShARCS	K_s	AO	⋯	0.588	3.272	4.774	5.816	6.625
	Shane (3 m)	ShARCS	J	AO	⋯	0.842	3.223	4.713	5.940	6.872
	WIYN (3.5 m)	NESSI	562 nm	Speckle	⋯	1.817	4.431	4.856	⋯	⋯
	WIYN (3.5 m)	NESSI	832 nm	Speckle	⋯	1.646	5.025	5.933	⋯	⋯
	SOAR (4.1 m)	HRCam	I_c	Speckle	⋯	1.903	5.370	5.629	5.887	6.145
731	Gemini-S (8 m)	DSSI	692 nm	Speckle	⋯	4.721	6.998	7.872	⋯	⋯
	Gemini-S (8 m)	DSSI	880 nm	Speckle	⋯	4.498	6.470	6.889	⋯	⋯
833	SOAR (4.1 m)	HRCam	I_c	Speckle	⋯	1.922	5.068	5.285	5.503	5.720
	Gemini-S (8 m)	Zorro	562 nm	Speckle	⋯	4.319	4.752	4.932	⋯	⋯
	Gemini-S (8 m)	Zorro	832 nm	Speckle	⋯	5.162	6.805	8.119	⋯	⋯
1075	SOAR (4.1 m)	HRCam	I_c	Speckle	⋯	1.708	4.990	5.310	5.631	5.9518
	Gemini-S (8 m)	Zorro	562 nm	Speckle	⋯	4.061	4.278	4.429	⋯	⋯
	Gemini-S (8 m)	Zorro	832 nm	Speckle	⋯	5.009	5.653	6.126	⋯	⋯
1242	CAHA (2.2 m)	AstraLux	SDSSz	Lucky	⋯	2.143	4.128	4.047	3.898	⋯
	Shane (3 m)	ShARCS	K_s	AO	Y	0.438	2.039	3.549	4.641	5.567
	Shane (3 m)	ShARCS	J	AO	Y	0.237	1.186	2.313	3.304	4.055
	Gemini-N (8 m)	'Alopeke	562 nm	Speckle	⋯	3.718	3.980	4.017	⋯	⋯
	Gemini-N (8 m)	'Alopeke	832 nm	Speckle	⋯	4.551	6.087	6.856	⋯	⋯
1263	WIYN (3.5 m)	NESSI	562 nm	Speckle	⋯	1.690	3.799	4.049	⋯	⋯
	WIYN (3.5 m)	NESSI	832 nm	Speckle	⋯	1.679	5.066	5.533	⋯	⋯
	SOAR (4.1 m)	HRCam	I_c	Speckle	Y	1.782	4.081	4.565	5.049	5.532
	Palomar (5 m)	PHARO	Brγ	AO	Y	1.716	6.869	8.648	9.145	9.275
	Palomar (5 m)	PHARO	Hcont	AO	Y	1.986	7.769	8.965	9.618	9.685
1411	CAHA (2.2 m)	AstraLux	SDSSz	Lucky	⋯	2.368	4.425	4.461	4.309	
	Palomar (5 m)	PHARO	Brγ	AO	⋯	1.789	6.912	8.190	9.017	9.241
	Gemini-N (8 m)	'Alopeke	562 nm	Speckle	⋯	4.333	5.609	5.877	⋯	⋯
	Gemini-N (8 m)	'Alopeke	832 nm	Speckle	⋯	4.414	7.160	8.496	⋯	⋯
	Keck (10 m)	NIRC2	K_s	AO	⋯	3.892	7.574	8.308	8.317	8.312
1442	Gemini-N (8 m)	'Alopeke	562 nm	Speckle	⋯	3.644	3.867	4.060	⋯	⋯
	Gemini-N (8 m)	'Alopeke	832 nm	Speckle	⋯	4.703	5.622	6.118	⋯	⋯
	Keck (10 m)	NIRC2	K	AO	⋯	3.905	7.638	7.801	7.837	7.782
1693	Shane (3 m)	ShARCS	K_s	AO	⋯	0.610	2.790	4.155	5.208	6.081
	Palomar (5 m)	PHARO	Brγ	AO	⋯	2.751	6.982	8.411	8.847	8.916
	Gemini-N (8 m)	'Alopeke	562 nm	Speckle	⋯	4.380	4.803	4.958	⋯	⋯
	Gemini-N (8 m)	'Alopeke	832 nm	Speckle	⋯	4.979	6.440	7.443	⋯	⋯
1860	Shane (3 m)	ShARCS	Brγ	AO	⋯	0.592	3.287	4.598	5.096	5.669
	Palomar (5 m)	PHARO	Brγ	AO	⋯	2.366	6.873	8.346	8.984	9.051
	Gemini-N (8 m)	'Alopeke	562 nm	Speckle	⋯	4.659	5.327	5.631	⋯	⋯
	Gemini-N (8 m)	'Alopeke	832 nm	Speckle	⋯	4.984	7.356	8.978	⋯	⋯
2260	CAHA (2.2 m)	AstraLux	SDSSz	Lucky	⋯	2.456	5.399	5.666	⋯	⋯
	SAI (2.5 m)	SPP	I_c	Speckle	⋯	2.548	5.293	6.406	⋯	⋯
	Shane (3 m)	ShARCS	K_s	AO	⋯	0.564	2.740	4.142	5.139	6.027
	Shane (3 m)	ShARCS	J	AO	⋯	0.547	2.345	3.799	5.040	5.968
	Palomar (5 m)	PHARO	Brγ	AO	⋯	2.875	6.920	8.418	8.983	9.106
	Gemini-N (8 m)	'Alopeke	562 nm	Speckle	⋯	4.688	5.674	6.283	⋯	⋯
	Gemini-N (8 m)	'Alopeke	832 nm	Speckle	⋯	4.539	6.577	8.384	⋯	⋯

Table 4
(Continued)

TOI	Telescope	Instrument	Filter	Image Type	Companion ($<5''$)	Contrast (Δmag)				
						$0''\!\!.1$	$0''\!\!.5$	$1''\!\!.0$	$1''\!\!.5$	$2''\!\!.0$
2290	SAI (2.5 m)	SPP	I_c	Speckle	⋯	1.207	5.176	6.509	⋯	⋯
	Gemini-N (8 m)	'Alopeke	562 nm	Speckle	⋯	3.740	4.231	4.424	⋯	⋯
	Gemini-N (8 m)	'Alopeke	832 nm	Speckle	⋯	4.965	6.128	7.071	⋯	⋯
	Keck (10 m)	NIRC2	K	AO	⋯	3.755	7.169	7.276	7.254	7.181
2411	SOAR (4.1 m)	HRCam	I_c	Speckle	⋯	1.844	5.776	6.031	6.286	6.541
	Palomar (5 m)	PHARO	Brγ	AO	⋯	2.566	7.197	8.199	8.637	8.712
	Keck (10 m)	NIRC2	Brγ	AO	⋯	3.906	6.505	6.552	6.476	6.483
2427	SOAR (4.1 m)	HRCam	I_c	Speckle	⋯	1.955	5.434	5.758	6.083	6.408
	Keck (10 m)	NIRC2	Brγ	AO	⋯	3.949	5.908	5.972	5.891	5.922
2445	Palomar (5 m)	PHARO	Brγ	AO	⋯	2.608	6.876	7.527	7.571	7.623
	Keck (10 m)	NIRC2	K	AO	⋯	3.955	6.939	6.904	6.912	6.895

4.1.3. WIYN/NESSI

We observed TOI-544 and TOI-1263 on UT 2019 October 12 and 2019 November 16, respectively, with the NN-Explore Exoplanet Stellar Speckle Imager (NESSI; Scott et al. 2018; Scott & Howell 2018) mounted on the 3.5 m WIYN telescope at Kitt Peak. High-speed electron-multiplying CCDs were used to capture image sequences simultaneously in two passbands at 562 and 832 nm. Data were acquired and reduced following Howell et al. (2011), yielding the 5σ contrast curves shown in Figure 2. No secondary sources were detected within the reconstructed $4''\!\!.6 \times 4''\!\!.6$ images.

4.1.4. SOAR/HRCam

We utilize speckle interferometric observations of TOI-206, TOI-500, TOI-539, TOI-544, TOI-833, TOI-1075, TOI-1263, and TOI-1427 taken with HRCam mounted on the 4.1 m Southern Astrophysical Research (SOAR) telescope. These observations and their related analyses are outlined in Ziegler et al. (2019, 2021). We refer the reader to those papers for more information.

4.1.5. Shane/ShARCS

We observed TOI-544, TOI-1242, TOI-1693, TOI-1860, and TOI-2260 using the ShARCS camera on the Shane 3 m telescope at Lick Observatory (Kupke et al. 2012; Gavel et al. 2014) on UT 2019 September 13, 2021 March 5, 2020 December 2, 2020 December 2, and 2021 March 29, respectively. Observations were taken using the Shane adaptive optics (AO) system in natural guide star mode. We collected our observations using a four-point dither pattern with a separation of $4''$ between each dither position. For TOI-544, TOI-1242, and TOI-2260 we obtained observations with the K_s filter ($\lambda_o = 2.150$; $\Delta\lambda = 0.320\ \mu$m) and the J filter ($\lambda_o = 1.238$; $\Delta\lambda = 0.271\ \mu$m). For TOI-1242, we detected a $\sim4''\!\!.3$ companion in both filters. For TOI-1693 we obtained observations with only the K_s filter. For TOI-1860 we obtained observations with only the narrowband Brγ filter ($\lambda_o = 2.167$; $\Delta\lambda = 0.020\ \mu$m). See Savel et al. (2020) for a detailed description of the observing strategy and reduction procedure.

4.1.6. Palomar/PHARO

The Palomar Observatory observations of TOI-1263, TOI-1693, TOI-1860, TOI-1411, TOI-2260, TOI-2411, and TOI-2445 were made with the PHARO instrument (Hayward et al. 2001) behind the natural guide star AO system P3K (Dekany et al. 2013) on UT 2019 June 13, 2021 September 19, 2021 June 21, 2020 January 8, 2021 March 3, 2021 August 23, and 2021 September 20, respectively, in a standard five-point quincunx dither pattern with steps of $5''$. Each dither position was observed three times, offset in position from each other by $0''\!\!.5$, for a total of 15 frames. The camera was in the narrow-angle mode with a full FOV of $\sim25''$ and a pixel scale of approximately $0''\!\!.025$ per pixel. Observations were made in the narrowband Brγ filter ($\lambda_o = 2.1686$; $\Delta\lambda = 0.0326\ \mu$m) for the three targets. TOI-1263, which was detected to have a $\sim2''\!\!.6$ companion, was also observed in the Hcont ($\lambda_o = 1.668$; $\Delta\lambda = 0.018\ \mu$m) filter to enable a color-based determination of the boundedness (Lund & Ciardi 2020).

The AO data were processed and analyzed with a custom set of IDL tools. The science frames were flat-fielded and sky-subtracted. The flat fields were generated from a median average of dark subtracted flats taken on sky. The flats were normalized such that the median value of the flats is unity. The sky frames were generated from the median average of the 15 dithered science frames; each science image was then sky-subtracted and flat-fielded. The reduced science frames were combined into a single combined image using an intrapixel interpolation that conserves flux, shifts the individual dithered frames by the appropriate fractional pixels, and median-coadds the frames. The final resolution of the combined dither was determined from the FWHHM of the point-spread function, which was typically $0''\!\!.1$.

4.1.7. Gemini-N/'Alopeke, Gemini-S/Zorro, and Gemini-S/DSSI

For TOI-206, TOI-500, TOI-833, TOI-1075, TOI-1242, TOI-1411, TOI-1442, TOI-1634, TOI-1693, TOI-1860, TOI-2260, and TOI-2290, speckle interferometric observations were performed using 'Alopeke and Zorro, dual-channel high-resolution imaging instruments mounted on the Gemini 8 m North and South telescopes, respectively (Scott & Howell 2018).[84] Those

---

[84] https://www.gemini.edu/instrumentation/current-instruments/alopeke-zorro/
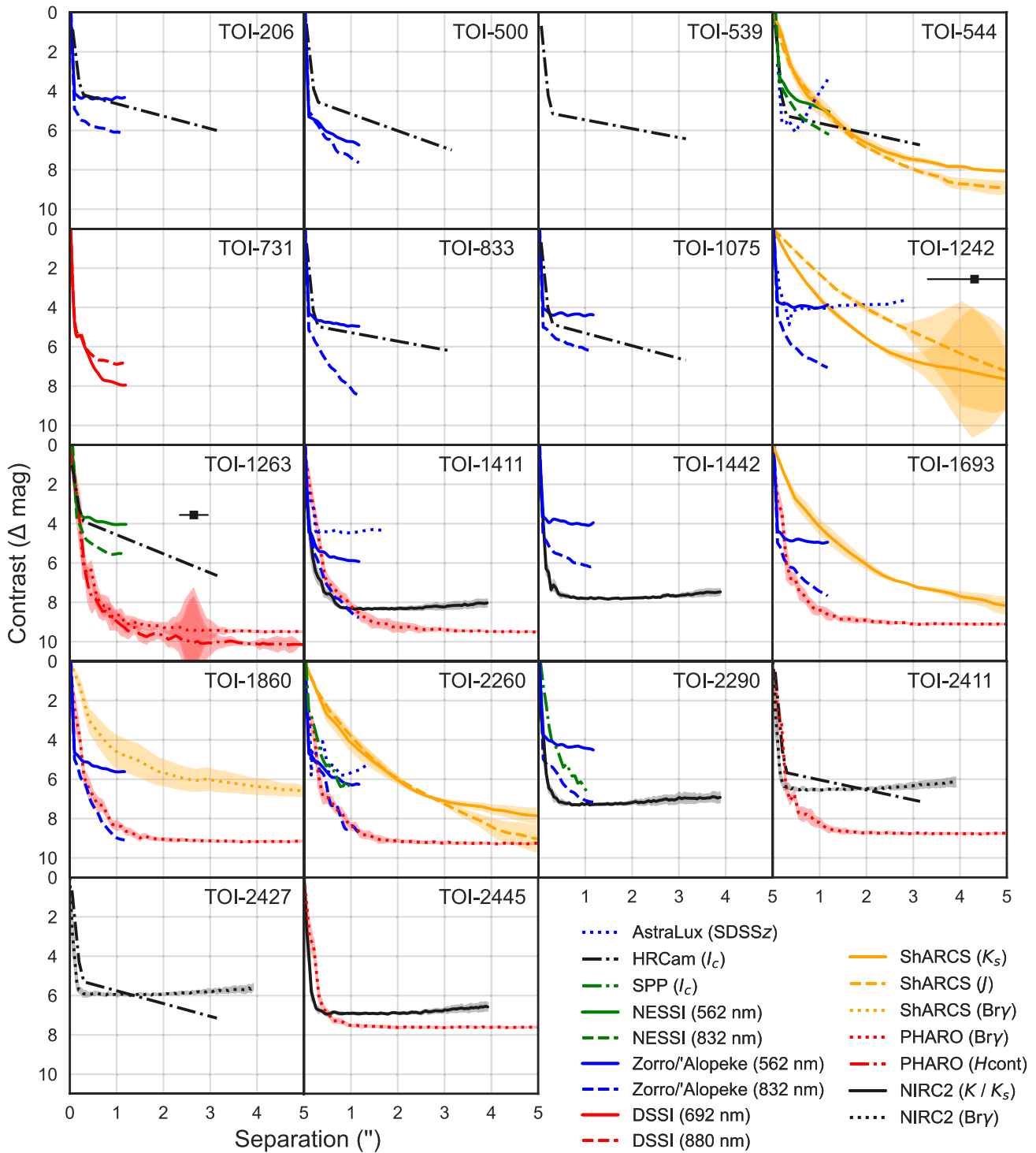
Figure 2. Contrast curves extracted from the high-resolution follow-up observations summarized in Table 4, which allows us to rule out companions at a given separation above a certain Δmag. Curves without shading (i.e., those from lucky and speckle imaging) were constructing by taking the 5σ upper limits of the contrasts in circular annuli around the target star. Curves with shading (i.e., those from adaptive optics imaging) were constructed by taking the mean and rms error of the contrasts in circular annuli around the target star. TOI-1242 and TOI-1263 have <5″ companions, which are both known stars in the TIC. The TESS band Δmag and separations of these companions are indicated by black squares. These curves are folded into the TRICERATOPS analysis described in Section 3.

observations were obtained on UT 2020 December 26, 2020 March 16, 2020 January 12, 2019 September 12, 2020 February 17, 2020 June 7, 2020 June 7, 2020 December 2, 2020 February 18, 2020 June 8, 2021 June 24, and 2021 June 24, respectively.

Many thousands of 60 ms images were collected on two EMCCDs, each preceded by a narrowband filter to minimize

atmospheric dispersion. The full set of observations taken in 562 nm and 832 nm was then combined in Fourier space to produce their power spectrum and autocorrelation functions. From these, interferometric fringes were detected if a companion star was present within our ~1″2 FOV, with an inner angle at the diffraction limit of the Gemini telescope. The data reduction pipeline produces final data products that

include 5σ contrast curves and reconstructed images (Horch et al. 1996, 2012; Howell et al. 2011). The contrast curves at both 562 nm and 832 nm sample the spatial region near the target star from approximately 1 au to 50–100 au (depending on the distance to the target star), yielding contrast levels of 5–8 mag.

For TOI-731, speckle interferometric observations were performed using the Differential Speckle Survey Instrument (DSSI; Horch et al. 2009), a dual-channel, high-resolution imager that allows simultaneous observations with filters centered at 692 nm and 880 nm. DSSI can resolve binaries down to 20 mas. The observations were obtained on UT 2018 March 30 when DSSI was mounted on the Gemini-South 8 m telescope as a visiting instrument.

4.1.8. Keck/NIRC2

TOI-1411, TOI-1442, TOI-2290, TOI-2411, TOI-2427, and TOI-2445 were observed with the NIRC2 instrument on Keck II behind the natural guide star AO system on UT 2020 September 9, 2020 May 28, 2021 August 28, 2021 August 28, 2021 August 24, and 2021 August 28, respectively. The observations were made in the standard three-point dither pattern that is used with NIRC2 to avoid the left lower quadrant of the detector, which is typically noisier than the other three quadrants. The dither pattern step size was $3''$ and was repeated two times offset from each other by $0\rlap{.}''5$, for a total of nine dithered observations. The observations for TOI-1411 were made in the K_s filter ($\lambda_o = 2.146; \Delta\lambda = 0.311\ \mu$m) and TOI-1442 were made in the K ($\lambda_o = 2.196; \Delta\lambda = 0.336\ \mu$m) filter. The camera was in the narrow-angle mode with a full FOV of $\sim 10''$ and a pixel scale of approximately $0\rlap{.}''099442$ per pixel. The Keck AO observations revealed no additional stellar companions to within a resolution of $\sim 0\rlap{.}''05$ FWHM. The data were processed and analyzed with the same software suite used for the Palomar PHARO observations.

4.2. Reconnaissance Spectroscopy

We obtained reconnaissance spectra of several of our TOIs to search for evidence of FPs and characterize the target stars. These spectra were obtained by members of TFOP Sub Group 2 (SG2). The observations and the stellar parameters extracted from the acquired spectra are summarized in Table 5. Further details on the observations and the analyses performed to search for FP signatures and characterize the stars are provided below.

4.2.1. FLWO/TRES and NOT/FIES

We obtained reconnaissance spectra of TOI-544, TOI-1242, TOI-1263, TOI-1411, TOI-1693, TOI-2290, TOI-2411, and TOI-2427 using the Tillinghast Reflector Echelle Spectrograph (TRES; Fűrész 2008) on the 1.5 m Tillinghast Reflector at the Fred L. Whipple Observatory (FLWO) on Mt. Hopkins, AZ. We also obtained reconnaissance spectra of TOI-1263, and TOI-1860 using the high-resolution FIbre-fed Echelle Spectrograph (FIES; Telting et al. 2014) at the 2.56 m Nordic Optical Telescope (NOT) on La Palma, Spain. We analyzed the TRES and FIES spectra in order to rule out spectroscopic binaries and to confirm that the assumed luminosity classes were correct.

The TRES and FIES reconnaissance spectroscopic observations were analyzed using the Stellar Parameter Classification

tool (SPC; Buchhave et al. 2012). In brief, SPC uses a correlation analysis of the observed spectra against a library of synthetic spectra calculated using Kurucz model atmospheres (Kurucz 1993). SPC fits for the $T_{\rm eff}$, $\log g$, [M/H], and projected rotational velocity ($v \sin i$) that give the highest peak correlation value using a multidimensional fit. We ran SPC with priors from the Yonsei−Yale isochrones on the fit (Yi et al. 2001). The library of calculated spectra used by SPC covers the following ranges: $3500\ {\rm K} < T_{\rm eff} < 9750\ {\rm K}$, $0.0 < \log g < 5.0$ (cgs), $-2.5 < [{\rm m/H}] < +0.5$, and $0\ {\rm km\ s^{-1}} < v \sin i < 200\ {\rm km\ s^{-1}}$ (Buchhave et al. 2012). SPC is optimized for slow-rotating solar-type stars. Because it was not designed to classify cool stars ($T_{\rm eff} \lesssim 4000\ {\rm K}$), for TOI-544, TOI-1693, TOI-2290, TOI-2411, and TOI-2427, we used empirical relations in order to estimate the stellar parameters (see Section 2.2 for more information).

4.2.2. SMARTS/CHIRON

We obtained reconnaissance spectra of TOI-500, TOI-539, TOI-544, TOI-731, TOI-833, TOI-1075, TOI-2411, and TOI-2427 using the CHIRON spectrograph on the 1.5 m SMARTS telescope, located at Cerro Tololo Inter-American Observatory (CTIO), Chile (Tokovinin et al. 2013). The spectra were analyzed using a machine-learning procedure based on $\sim$10,000 TRES spectra classified by SPC and interpolated via a gradient boosting regressor that provides estimates of $T_{\rm eff}$, $\log g$, [M/H], and $v \sin i$. These classifications therefore suffer the same limitations as SPC for the coolest stars, so we estimate parameters for TOI-544, TOI-731, TOI-833, TOI-1075, TOI-2411, and TOI-2427 using the same empirical relations described in Section 2.2. The spectra for all four TOIs have cross-correlation profiles indicative of a single star and no significant RV variations.

4.2.3. Keck/HIRES

We obtained reconnaissance spectra of TOI-1242, TOI-1411, TOI-1693, TOI-1860, TOI-2260, and TOI-2290 using the High Resolution Echelle Spectrometer (HIRES; Vogt et al. 1994) mounted on the Keck I 10 m telescope on Maunakea. Our HIRES spectra were analyzed to rule out double-lined spectroscopic binaries and confirm that the stars are not giants. To do the former, we used ReaMatch (Kolbl et al. 2014), which can identify double-line spectroscopic binaries with contamination ratios as small as 1% to constrain the presence of unresolved binary stars near each TOI. To do the latter, we classified each star using SpecMatch Synthetic (Petigura 2015) and SpecMatch Empirical (Yee et al. 2017). SpecMatch Synthetic classifies stars by searching a multidimensional grid of synthetic spectra for that which best matches the observed spectrum. SpecMatch Empirical works similarly but instead compares the observed spectrum to a library of spectra of well-characterized stars. The former provides estimates for $T_{\rm eff}$, $\log g$, $M_\star$, $R_\star$, [Fe/H], and $v \sin i$, while the latter provides estimates for $T_{\rm eff}$, $R_\star$, and [Fe/H]. Because SpecMatch Empirical outperforms SpecMatch Synthetic for cooler stars, we adopt the SpecMatch Empirical results for stars that SpecMatch Empirical determines to have $T_{\rm eff} < 4700\ {\rm K}$, and we adopt the SpecMatch Synthetic results for stars that SpecMatch Empirical determines to have $T_{\rm eff} > 4700\ {\rm K}$.

In addition, we estimated the activity levels of targets observed with HIRES by calculating their $\log R'_{\rm H\,K}$ values

Table 5
Summary of Reconnaissance Spectroscopy Follow-up and Derived Stellar Parameters

TOI	Telescope	Instrument	N_{obs}	T_{eff} (K)	$\log g$	$M_\star$ ($M_\odot$)	$R_\star$ ($R_\oplus$)	[Fe/H]	[M/H]	$v \sin i$ (km s^{-1})
500	SMARTS (1.5 m)	CHIRON	2	4621 ± 50	4.63 ± 0.10	⋯	⋯	⋯	-0.22 ± 0.10	2.00 ± 0.50
539	SMARTS (1.5 m)	CHIRON	2	5031 ± 50	4.58 ± 0.10	⋯	⋯	⋯	-0.14 ± 0.10	3.30 ± 0.50
544	SMARTS (1.5 m)	CHIRON	4	⋯	⋯	⋯	⋯	⋯	⋯	⋯
	FLWO (1.5 m)	TRES	2	4369 ± 100	4.73 ± 0.10	⋯	⋯	⋯	-0.42 ± 0.08	1.80 ± 0.50
731	SMARTS (1.5 m)	CHIRON	2	⋯	⋯	⋯	⋯	⋯	⋯	⋯
833	SMARTS (1.5 m)	CHIRON	2	⋯	⋯	⋯	⋯	⋯	⋯	⋯
1075	SMARTS (1.5 m)	CHIRON	1	⋯	⋯	⋯	⋯	⋯	⋯	⋯
1242	FLWO (1.5 m)	TRES	2	4437 ± 100	4.69 ± 0.10	⋯	⋯	⋯	-0.13 ± 0.08	3.60 ± 0.50
	Keck (10 m)	HIRES	2	4259 ± 70	⋯	⋯	0.68 ± 0.10	0.00 ± 0.09	⋯	⋯
1263	FLWO (1.5 m)	TRES	1	5160 ± 50	4.58 ± 0.10	⋯	⋯	⋯	0.04 ± 0.08	2.10 ± 0.50
	NOT (2.56 m)	FIES	4	5172 ± 50	4.50 ± 0.10	⋯	⋯	⋯	0.00 ± 0.08	0.60 ± 0.50
1411	FLWO (1.5 m)	TRES	2	4352 ± 100	4.73 ± 0.10	⋯	⋯	⋯	-0.37 ± 0.08	2.00 ± 0.50
	Keck (10 m)	HIRES	2	4180 ± 70	⋯	⋯	0.66 ± 0.10	0.10 ± 0.09	⋯	⋯
1693	FLWO (1.5 m)	TRES	2	⋯	⋯	⋯	⋯	⋯	⋯	⋯
	Keck (10 m)	HIRES	1	3466 ± 70	⋯	⋯	0.44 ± 0.10	0.03 ± 0.09	⋯	⋯
1860	NOT (2.56 m)	FIES	1	5780 ± 50	4.54 ± 0.10	⋯	⋯	⋯	-0.09 ± 0.08	11.10 ± 0.50
	Keck (10 m)	HIRES	1	5724 ± 100	4.61 ± 0.10	0.99 ± 0.03	0.94 ± 0.02	0.04 ± 0.06	⋯	10.37 ± 1.00
2260	Keck (10 m)	HIRES	1	5534 ± 100	4.62 ± 0.10	0.99 ± 0.04	0.94 ± 0.05	0.22 ± 0.06	⋯	5.05 ± 1.00
2290	FLWO (1.5 m)	TRES	2	⋯	⋯	⋯	⋯	⋯	⋯	⋯
	Keck (10 m)	HIRES	1	3813 ± 70	⋯	⋯	0.57 ± 0.10	-0.03 ± 0.09	⋯	⋯
2411	SMARTS (1.5 m)	CHIRON	3	⋯	⋯	⋯	⋯	⋯	⋯	⋯
	FLWO (1.5 m)	TRES	2	⋯	⋯	⋯	⋯	⋯	⋯	⋯
2427	SMARTS (1.5 m)	CHIRON	2	⋯	⋯	⋯	⋯	⋯	⋯	⋯
	FLWO (1.5 m)	TRES	2	⋯	⋯	⋯	⋯	⋯	⋯	⋯

Note. Spectrum-derived parameters for each TOI. Entries that list no stellar parameters correspond to stars too cool to have parameters extracted using data collected with the specified instrument. More details on how these parameters were derived are in Section 4.2.

(Linsky et al. 1979). In general, stars with higher $\log R'_{H K}$ values are younger and more active. Rotationally modulated starspots on active stars introduce more scatter in RV observations, making planet mass measurement more difficult (Hillenbrand et al. 2014). This quantity is therefore useful for planning future planet characterization efforts.

Lastly, we measured 15 elemental abundances for two stars (TOI-1860 and TOI-2260) using the KeckSpec algorithm (Rice & Brewer 2020) on our high-S/N HIRES spectra. This algorithm is able to reliably measure abundances for stars with $T_{eff} > 4700$ K. The spectra were reduced, extracted, and calibrated following the standard approach of the California Planet Search consortium (Howard et al. 2010). We then interpolated the spectra onto the wavelength grid required for KeckSpec before feeding them to the algorithm. The resulting abundances are shown in Table 6. Because elemental abundances are believed to influence the compositions of planet interior and atmospheres (e.g., Bond et al. 2010;

Konopacky et al. 2013; Moriarty et al. 2014), the quantities may be useful when characterizing these planets and their systems in the future.

4.3. Time-series Photometry

To determine whether or not the signal observed by TESS is on the presumed target star and to help eliminate FPs from blends, we compile a set of observations collected by members of TFOP Sub Group 1 (SG1). These follow-up observations were scheduled using the TESS Transit Finder, which is a customized version of the Tapir software package (Jensen 2013). A summary of these observations is given in Table 7 and details about the facilities used are given in Table 8.

We search for transits around the target stars in our observations using the Bayesian Information (Schwarz 1978), considering a transit detected if a transit model is preferred over

Table 6
Elemental Abundances Derived with KeckSpec

TOI	[C/H]	[N/H]	[O/H]	[Na/H]	[Mg/H]	[Al/H]	[Si/H]	[Ca/H]	[Ti/H]	[V/H]	[Cr/H]	[Mn/H]	[Fe/H]	[Ni/H]	[Y/H]
1860	0.04	−0.05	0.15	−0.05	−0.03	−0.06	0.00	0.14	0.09	0.09	0.09	0.02	0.09	−0.02	0.17
2260	0.01	−0.03	0.07	0.02	0.01	0.02	0.08	0.20	0.08	0.08	0.16	0.12	0.16	0.07	0.26
Error	0.07	0.09	0.09	0.07	0.04	0.08	0.06	0.07	0.05	0.07	0.05	0.07	0.05	0.05	0.09

Note. The bottom row contains the systematic uncertainty for each abundance.

Table 7
Summary of Time-series Photometry Follow-up

TOI	TIC ID	Telescope	Date (UT)	Filter(s)
206.01	55650590	LCO 1.0 m	2018-11-19	r'
		SLR2	2018-11-22	V
		LCO 1.0 m	2018-11-23	i'
		CKD700	2018-11-30	r'
		LCO 1.0 m	2018-12-01	$r'i'$
		LCO 1.0 m	2018-12-02	i'
		LCO 1.0 m	2018-12-06	r'
		LCO 1.0 m	2018-12-09	i'
500.01	134200185	LCO 1.0 m	2019-03-15	r'
		TRAPPIST-S.	2019-03-24	B
		LCO 0.4 m	2019-03-30	i'
		PEST	2019-03-30	R_c
		LCO 1.0 m	2019-05-02	z_s
539.01	238004786	PEST	2019-03-29	R_c
		MKO CDK700	2019-03-31	r'
		LCO 1.0 m	2019-04-06	i'
		LCO 1.0 m	2019-04-08	z_s
		LCO 1.0 m	2019-04-17	i'
544.01	50618703	LCO 1.0 m	2019-09-20	z_s
		TCS	2019-10-13	$g'r'i'$
731.01	34068865	LCO 1.0 m	2019-06-10	V
		MKO CDK700	2019-06-11	i'
		PEST	2020-01-05	R_c
		LCO 1.0 m	2020-05-12	z_s
833.01	362249359	LCO 1.0 m	2020-03-28	z_s
		LCO 1.0 m	2020-05-14	z_s
		MKO CDK700	2020-05-15	i'
1075.01	351601843	LCO 1.0 m	2019-08-25	z_s
		LCO 1.0 m	2019-08-26	z_s
		MEarth-S	2019-09-22	RG715
		LCO 1.0 m	2019-09-23	z_s
		LCO 1.0 m	2019-09-24	z_s
		LCO 1.0 m	2019-09-26	z_s
		MEarth-S	2019-09-28	RG715
1242.01	198212955	TCS	2020-01-27	$g'r'i'z_s$
		TCS	2020-02-01	$g'r'i'z_s$
		TCS	2020-02-09	$g'r'i'z_s$
		ULMT	2020-05-18	i'
		TCS	2020-06-09	$g'r'i'z_s$
1263.01	406672232	LCO 1.0 m	2020-06-15	z_s
		LCO 1.0 m	2020-07-28	z_s
1411.01	116483514	LCO 1.0 m	2020-02-28	i'
		DSW CDK500	2020-04-16	r'
		TCS	2020-04-21	$g'r'i'z_s$
		LCO 1.0 m	2020-04-29	r'
		ULMT	2020-05-02	i'
		TCS	2020-05-10	$g'r'i'z_s$
1442.01	235683377	OMM 1.6 m	2020-02-09	i'
		LCO 1.0 m	2020-08-14	i'
		LCO 1.0 m	2020-08-30	I_c
		LCO 1.0 m	2020-09-26	i'
		LCO 2.0 m	2021-05-21	$g'r'i'z_s$
		LCO 2.0 m	2021-06-06	$g'r'i'z_s$
		LCO 2.0 m	2021-06-17	$g'r'i'z_s$
1693.01	353475866	LCO 1.0 m	2020-02-14	z_s
		LCO 1.0 m	2020-10-11	z_s
		TCS	2020-09-18	$g'i'z_s$

Table 7
(Continued)

TOI	TIC ID	Telescope	Date (UT)	Filter(s)
1860.01	202426247	Adams	2020-06-06	I_c
		TCS	2020-07-20	$g'r'i'z_s$
2260.01	232568235	TRAPPIST-N	2020-09-28	z'
		Adams	2021-06-26	I_c
2290.01	321688498	LCO 1.0 m	2020-10-15	i'
2411.01	10837041	MKO CDK700	2021-01-13	i'
		LCO 1.0 m	2021-06-19	r'
		LCO 1.0 m	2021-07-10	i'
		LCO 1.0 m	2021-07-25	i'
		LCO 1.0 m	2021-08-27	i'
		LCO 1.0 m	2021-08-29	i'
		LCO 1.0 m	2021-08-30	i'
		LCO 1.0 m	2021-09-09	i'
2427.01	142937186	PEST	2021-01-12	R_c
		LCO 1.0 m	2021-01-30	z_s
		LCO 1.0 m	2021-02-22	z_s
		LCO 1.0 m	2021-08-14	z_s
		LCO 1.0 m	2021-08-17	z_s
2445.01	439867639	MLO	2021-01-10	I_c
		TRAPPIST-S	2021-01-08	$I + z$
		TRAPPIST-S	2021-01-14	$I + z$
		NAOJ 188 cm	2021-02-07	$g'r'z_s$

a flat line. For several of our TOIs, transits were verified on target using these observations. These cases are further described below. We incorporate these data into the transit fits described in Section 2.3 to obtain tighter constraints on the ephemerides of the planet candidates.

4.3.1. LCO 1.0 m/Sinistro

We observed full transits of TOI-206.01, TOI-1075.01, TOI-1442.01, TOI-1693.01, TOI-2411.01, and TOI-2427.01 using the Sinistro cameras on the Las Cumbres Observatory (LCO) 1.0 m telescopes. Images were calibrated by the standard LCOGT BANZAI pipeline (McCully et al. 2018), and the photometric data were extracted using the AstroImageJ (AIJ) software package (Collins et al. 2017). (Brown et al. 2013).

Transits of TOI-206.01 were observed with an i' filter on UT 2018 November 23, 2018 December 1, and 2018 December 9 and were found to have a depth of ∼1.0–1.5 ppt. Transits of TOI-1075.01 were observed with a z_s filter on UT 2019 August 26, 2019 September 23, 2019 September 24, and 2019 September 26 and were found to have a depth of ∼0.5–1.0 ppt. Transits of TOI-1442.01 were observed with an i' filter on UT 2020 August 14, 2020 September 26, and 2020 October 21 and were found to have a depth of ∼1.0–2.0 ppt. Transits of TOI-1693.01 were observed with a z_s filter on UT 2020 February 14 and 2020 October 11 and were found to have a depth of ∼0.5–1.0 ppt. Transits of TOI-2441.01 were observed with an i' filter on UT 2021 July 10, 2021 July 25, 2021 August 27, 2021 August 29, 2021 August 30, and 2021 September 9 and were found to have a depth of ∼0.25–0.75 ppt. Transits of TOI-2427.01 were observed with a z_s filter on UT 2021 August 14 and 2021 August 17 and were found to have a depth of

Table 8
Facilities Used for TFOP SG1 Follow-up

Observatory	Telescope/Instrument	Aperture (m)	Pixel Scale (arcsec)	FOV (arcmin)
Austin College Adams Observatory (Adams)	⋯	0.61	0.38	26 × 26
Cerro Tololo Inter-American Observatory	MEarth-South	0.4	0.84	29 × 29
Deep Sky West Remote Observatory (DSW)	DSW CDK500	0.5	1.09	37 × 37
Las Cumbres Observatory (LCO)	LCO 0.4 m / SBIG-6303	0.4	0.57	29.2 × 19.5
Las Cumbres Observatory (LCO)	LCO 1.0 m / Sinistro	1.0	0.39	26.5 × 26.5
Haleakala Observatory	LCO 2.0 m / MuSCAT3	2.0	0.27	9.1 × 9.1
Maury Lewin Astronomical Observatory (MLO)	⋯	0.36	0.84	23 × 17
Mt. Kent Observatory (MKO)	MKO CDK700	0.7	0.4	27 × 27
Observatoire du Mont-Mégantic (OMM)	OMM 1.6 m / PESTO	1.6	0.47	7.95 × 7.95
National Astronomical Observatory of Japan (NAOJ)	NAOJ 188 cm / MuSCAT	1.88	0.36	6.1 × 6.1
Oukaïmeden Observatory	TRAPPIST-North	0.6	0.64	22 × 22
South African Astronomical Observatory	SLR2	0.5	0.37	12 × 12
Teide Observatory	Telescopio Carlos Sánchez (TCS) / MuSCAT2	1.52	0.44	7.4 × 7.4
La Silla Observatory	TRAPPIST-South	0.6	0.64	22 × 22
Mt. Lemmon Observatory	Univ. of Louisville Manner Telescope (ULMT)	0.61	0.39	26 × 26
⋯	Perth Exoplanet Survey Telescope (PEST)	0.3	1.2	31 × 21

~0.25–0.75 ppt. The data for each of these TOIs can be seen in Figures 3–9.

4.3.2. MEarth-South

We observed full transits of TOI-1075.01 on UT 2019 September 22 and 2019 September 28 using the MEarth-South telescope array at the Cerro Tololo Inter-American Observatory (Nutzman & Charbonneau 2008; Irwin et al. 2015). The observations were collected with an RG715 filter and were found to have a transit depth of ~0.5–1.0 ppt. The data can be seen in Figure 4.

4.3.3. OMM 1.6 m/PESTO

We observed a full transit of TOI-1442.01 on UT 2020 February 9 using the PESTO camera installed at the 1.6 m Observatoire du Mont-Mégantic (OMM), Canada. PESTO is equipped with a 1024 × 1024 EMCCD detector with a scale of 0″466 per pixel, providing an FOV of 7′95 × 7′95. The observations were collected with an i' filter and with a 30 s exposure time. Image calibrations, including bias subtraction and flat-field correction, and differential aperture photometry were performed with `AstroImageJ` (Collins et al. 2017). The events were observed with an i' filter and were found to have a transit depth of ~1 ppt. The data can be seen in Figure 5.

4.3.4. TRAPPIST-South

We observed two full transits of TOI-2445.01 using the TRAPPIST-South telescope (Jehin et al. 2011; Gillon et al. 2011; Barkaoui et al. 2019) on UT 2021 January 8 and 2021 February 14. TRAPPIST-South is a 60 cm robotic telescope installed at La Silla observatory in Chile since 2010, and it is equipped with a thermoelectric 2Kx2K FLI ProLine PL3041-BB CCD camera with an FOV of 22′ × 22′ and a pixel scale of 0″65. Data calibration and photometric measurements were performed using the PROSE[85] pipeline (Garcia et al. 2021). Both events were observed in the $I + z$ filter and were found to have a transit depth of ~2.5 ppt. The data can be seen in Figure 10.

---

[85] https://github.com/lgrcia/prose
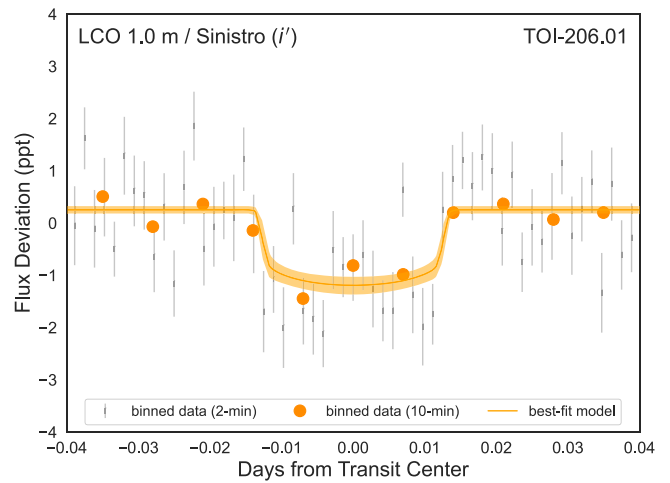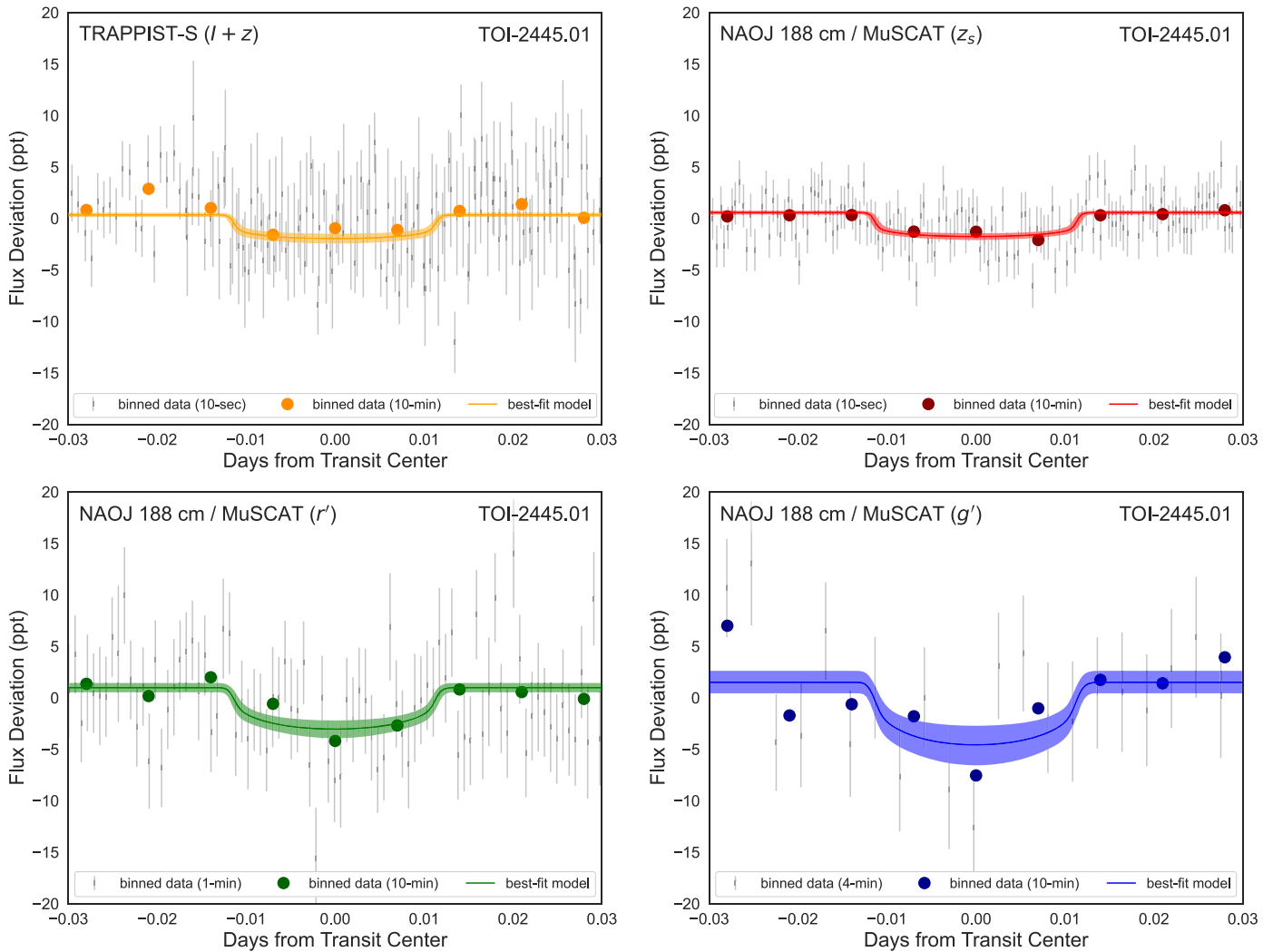

Figure 3. Phase-folded ground-based data and best-fit model of the transit of TOI-206.01. The data are detrended with a linear model and 3σ outliers are removed.

4.3.5. NAOJ 188 cm/MuSCAT, TCS/MuSCAT2, and LCO 2.0 m/MuSCAT3

We observed transits of TOI-1442.01, TOI-1693.01, and TOI-2445.01 using the MuSCAT, MuSCAT2, and MuSCAT3 instruments (Narita et al. 2015, 2019, 2020), which collect simultaneous observations using several filters. We observed full transits of TOI-1442.01 on UT 2021 May 21, 2021 June 6, and 2021 June 17 using MuSCAT3 on the LCO 2.0 m telescope at Haleakala Observatory. Observations were collected with the g', r', i', and z_s filters and measured a transit depth of ~1.0–2.0 ppt. We observed a full transit of TOI-1693.01 on UT 2020 September 18 using MuSCAT2 on the Telescopio Carlos Sánchez (TCS) at Teide Observatory. Observations were collected with g', i', and z_s filters and measured a transit depth of ~0.5–1.0 ppt. We observed a full transit of TOI-2445.01 on UT 2021 February 7 using MuSCAT on the National Astronomical Observatory of Japan (NAOJ) 188 cm telescope. Observations were collected with the g', r', and z_s filters and measured a transit depth of ~1.0–5.0 ppt. These data can be seen in Figure 5, Figure 6, and Figure 10.
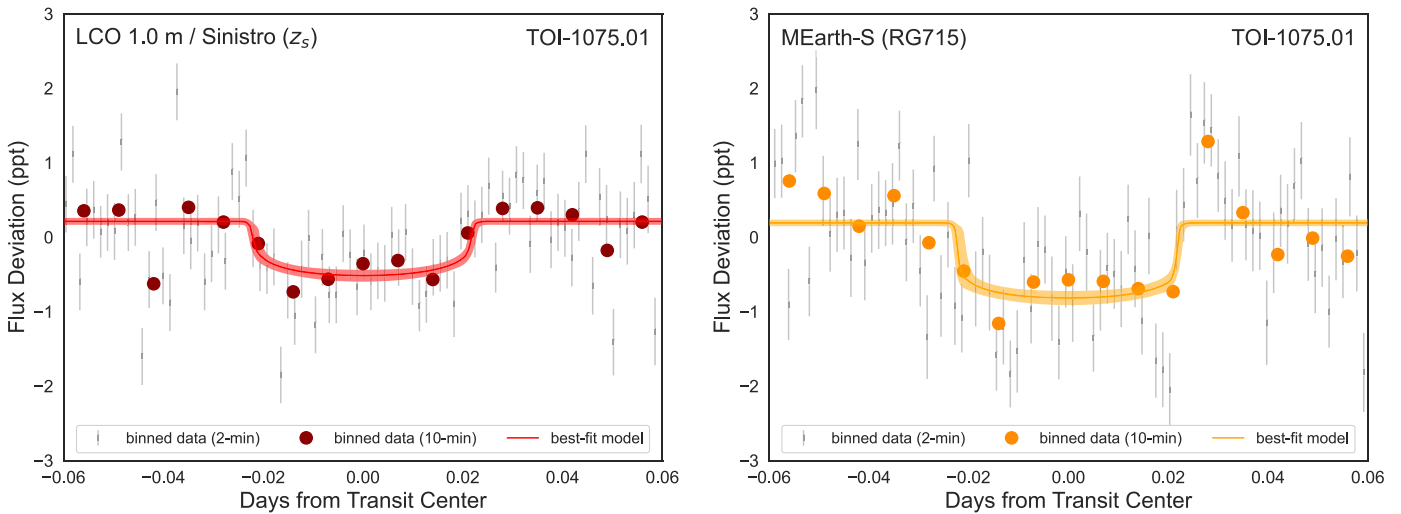
Figure 4. Phase-folded ground-based data and best-fit model of the transit of TOI-1075.01. The data are detrended with a linear model and 3σ outliers are removed.

5. Results

Below, we provide a brief summary of each of the planet candidates analyzed in this paper. We begin with details about the target stars, including their brightnesses, distances, and the TESS sectors in which they were observed. In addition, we analyze the available data of each star to search for activity indicators and signs of system youth. Specifically, we apply a Lomb–Scargle periodogram to each individual sector of TESS photometry to constrain the level of starspot variability. We consider the detection of photometric variability to be significant if the maximum peak calculated by the periodogram across all sectors is >0.5. When available, we also consider the spectrum-derived $v \sin i$ and $\log R'_{\rm HK}$.

Next, we present information gleaned from each step of our vetting process. We also summarize this information in Table 9. For TFOP SG3 high-resolution imaging observations, we refer to the TOI as "clear" if no stars were resolved within the detection limits stated in Figure 2. For TFOP SG2 reconnaissance spectroscopy observations, we refer to the TOI as "clear" if the target star was confirmed to be on the main sequence and no evidence of a spectroscopic binary was detected. For TFOP SG1 time-series photometry observations, we identified all stars from Gaia DR2 within $2\rlap{.}{''}5$ of the target star that are bright enough to cause the TESS transit detection based on the observed transit depth, the angular distance from the target star, and the difference in magnitude from the target star. For convenience, we refer to these as "neighbor stars" in the discussion below, and we describe them as "cleared" if our photometric follow-up observations showed that they have no transit-like events of the depth that would be necessary to reproduce the TESS event when blended with the central star.

At the end of each subsection, we decide whether the TOI is validated based on the results of the TRICERATOPS analysis. To forecast the potential of measuring the masses of the planet candidates via precise RVs, we also estimate the semiamplitude ($K_{\rm RV}$) and planet mass ($M_{\rm p}$) of each using the probabilistic planet mass–radius relation given in Chen & Kipping (2016) and the adopted stellar masses listed in Table 2. However, we stress that these estimates are merely illustrative, and should not be quoted as the actual masses and semiamplitudes.

5.1. TOI-206.01

TOI-206.01 is a $1.30 \pm 0.05 \, R_{\oplus}$ planet candidate with a 0.74 day orbital period orbiting an M dwarf (TIC 55650590) that is 47.7 pc away and has a V magnitude of 14.94. A Lomb–Scargle periodogram of the photometry from each TESS sector finds a maximum peak of 0.04, indicating that the star is quiet. TOI-206 has been observed in 26 TESS sectors (1–13 and 27–39).

Follow-up observations have found no evidence of this TOI being an FP, although no spectroscopic observations have been collected. Time-series photometric follow-up has made several detections of the transit of TOI-206.01 on TIC 55650590 (shown in Figure 3).

The DAVE analysis of this TOI detects a potential secondary eclipse in the TESS light curve, which could indicate that the transit is due to an eclipsing binary. Because follow-up observations do not detect a companion star that could dilute the radius of the transiting object and because the transit was detected on target, this eclipsing binary would need to have a grazing transit. The morphology of the transit shown in Figure 1 is inconsistent with that of a grazing eclipsing binary, meaning the feature detected in the TESS photometry is unlikely to be an actual secondary eclipse. The SPOC data validation report for this TOI reports no significant centroid offset.

The TRICERATOPS analysis of this TOI finds $FPP = (2.02 \pm 1.48) \times 10^{-5}$. Because all neighboring stars have been cleared, TRICERATOPS finds $NFPP = 0.0$. This FPP is sufficiently low to consider the planet validated. We hereafter refer to this planet as TOI-206 b.

We estimate the semiamplitude of the RV signal for this planet to be $K_{\rm RV} = 3.1^{+2.0}_{-1.0} \, {\rm m \, s^{-1}}$, corresponding to $M_{\rm p} = 2.2^{+1.4}_{-0.7} \, M_{\oplus}$.

5.2. TOI-500.01

TOI-500.01 is a $1.16 \pm 0.12 \, R_{\oplus}$ planet candidate with a 0.55 day orbital period orbiting a K dwarf (TIC 134200185) that is 47.4 pc away and has a V magnitude of 10.54. A Lomb–Scargle periodogram of the photometry from each TESS sector finds a maximum peak of 0.007, indicating that the star is quiet. This is corroborated by the low $v \sin i$ extracted from our CHIRON spectra. TOI-500 has been observed in six TESS sectors (6–8 and 33–35).

Follow-up observations have found no evidence of this TOI being an FP. Time-series photometric follow-up of this TOI has
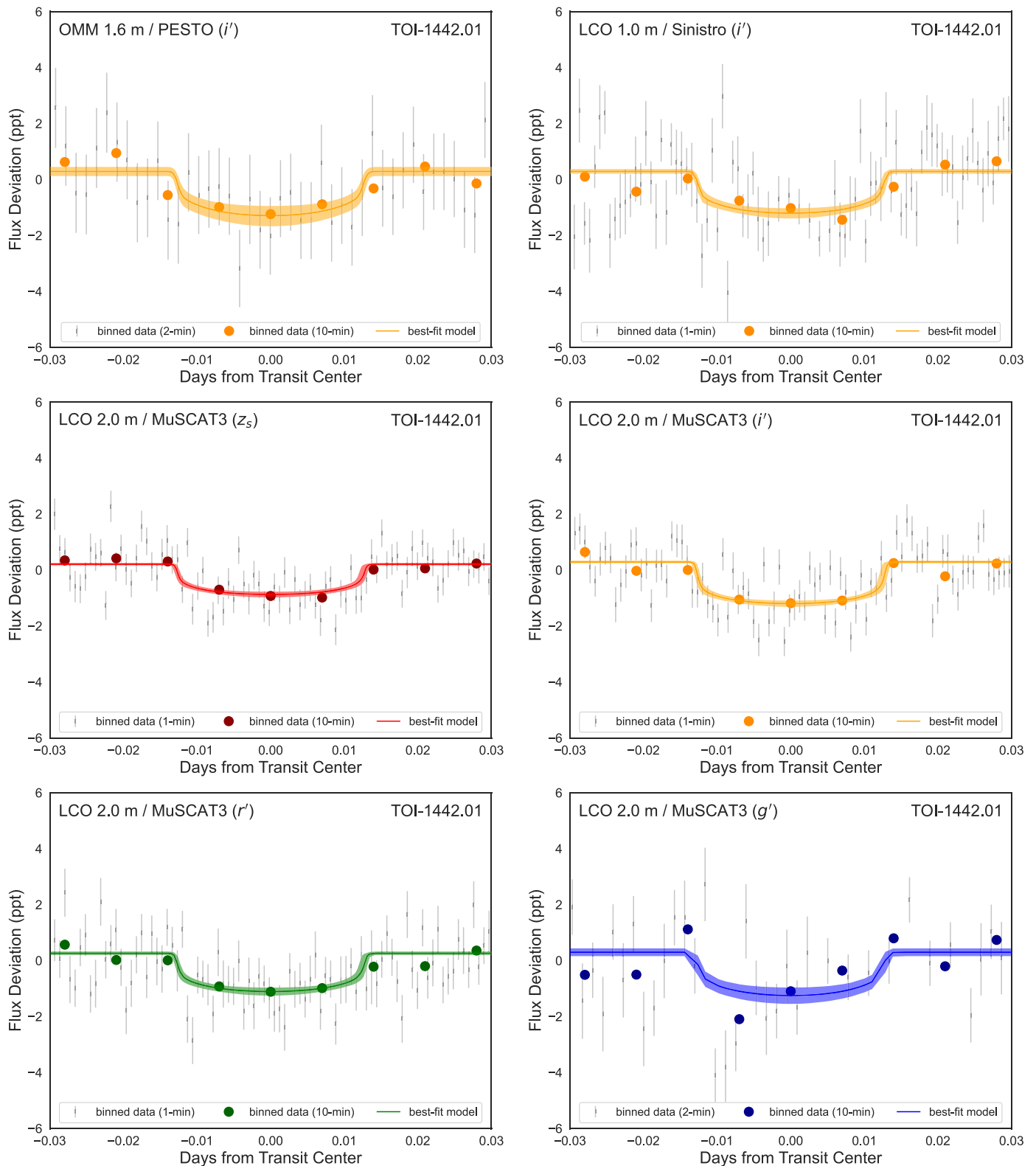
Figure 5. Phase-folded ground-based data and best-fit model of the transit of TOI-1442.01. The data are detrended with a linear model and 3σ outliers are removed.

cleared all neighboring stars as origins of the transit but has not yet detected the 0.23 ppt event seen in the TESS data around the target star.

DAVE finds no strong indicators that the candidate is an FP. We note, though, that the photocenter offset analysis performed by DAVE suffers from low S/N and poor quality in most of the

per-transit difference images. As a result, there is a large scatter in the measured photocenters for each individual transit, making it difficult for DAVE to detect a significant photocenter offset. The SPOC data validation report, however, does detect significant centroid offsets in sectors 8, 34, and 35. No offsets were detected in sectors 7 or 33 by SPOC, and no data
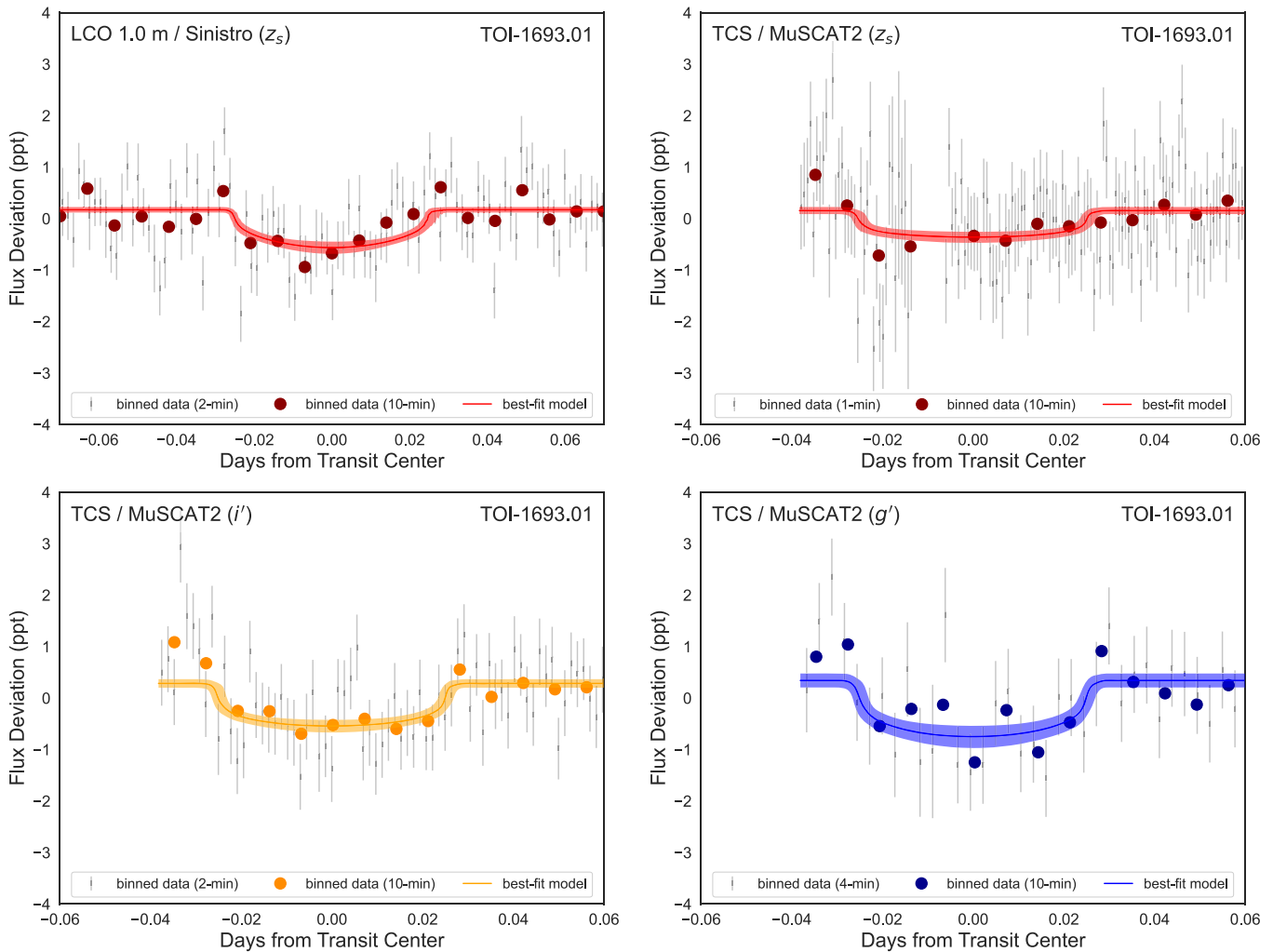
Figure 6. Phase-folded ground-based data and best-fit model of the transit of TOI-1693.01. The data are detrended with a linear model and 3σ outliers are removed.

validation report was generated by the SPOC pipeline for sector 6. Given that all neighboring stars have been cleared from being nearby eclipsing binaries, these offsets are unlikely to be caused by an FP originating from a nearby star.

The TRICERATOPS analysis of this TOI finds $\mathrm{FPP} = (7.12 \pm 1.13) \times 10^{-3}$. Because all neighboring stars have been cleared, TRICERATOPS finds $\mathrm{NFPP} = 0.0$. This FPP is sufficiently low to consider the planet validated. We hereafter refer to this planet as TOI-500 b.

We estimate the semiamplitude of the RV signal for this planet to be $K_{\mathrm{RV}} = 1.4^{+1.1}_{-0.7} \mathrm{\ m\ s}^{-1}$, corresponding to $M_{\mathrm{p}} = 1.6^{+1.3}_{-0.7} \, M_{\oplus}$.

5.3. TOI-539.01

TOI-539.01 is a $1.25 \pm 0.10 \, R_{\oplus}$ planet candidate with a 0.31 day orbital period orbiting a K dwarf (TIC 238004786) that is 108.4 pc away and has a V magnitude of 11.73. A Lomb–Scargle periodogram of the photometry from each TESS sector finds a maximum peak of 0.07, indicating that the star is quiet. This is corroborated by the low $v \sin i$ extracted from our CHIRON spectrum. TOI-539 has been observed in 11 TESS sectors (2, 6, 8, 9, 12, 29, 32–35, and 39).

Follow-up observations have found no evidence of this TOI being an F. Time-series photometric follow-up of this TOI has cleared all neighboring stars as origins of the transit except for

TIC 767067264, which is $7\rlap{.}''2$ west and 7.9 mag fainter in the Gaia G_{Rp} band. This nearby star appears not to show an event of the necessary depth but is not cleared at high confidence. The 0.31 ppt event seen in the TESS data has not been detected around the target star.

The DAVE analysis of this TOI finds no strong indicators that the candidate is an FP. However, like TOI-500 b, the per-transit difference images used by DAVE have very low S/N and the measured photocenters are unreliable. The SPOC data validation report for this TOI reports no significant centroid offset.

The TRICERATOPS analysis of this TOI finds $\mathrm{FPP} = (3.98 \pm 0.03) \times 10^{-2}$ and $\mathrm{NFPP} = (7.76 \pm 0.26) \times 10^{-22}$. This $>1\%$ FPP comes from the scenario that the TOI is a blended eclipsing binary. While this NFPP indicates that this TOI is unlikely to originate from the nearby star TIC 767067264, the FPP is too high to validate the planet candidate.

Assuming this is a real planet, we estimate the semiamplitude of its RV signal to be $K_{\mathrm{RV}} = 1.9^{+1.6}_{-0.7} \mathrm{\ m\ s}^{-1}$, corresponding to $M_{\mathrm{p}} = 1.9^{+1.6}_{-0.7} \, M_{\oplus}$.

5.4. TOI-544.01

TOI-544.01 is a $2.03 \pm 0.10 \, R_{\oplus}$ planet candidate with a 1.55 day orbital period orbiting a K dwarf (TIC 50618703) that is 41.1 pc away and has a V magnitude of 10.78. A Lomb–
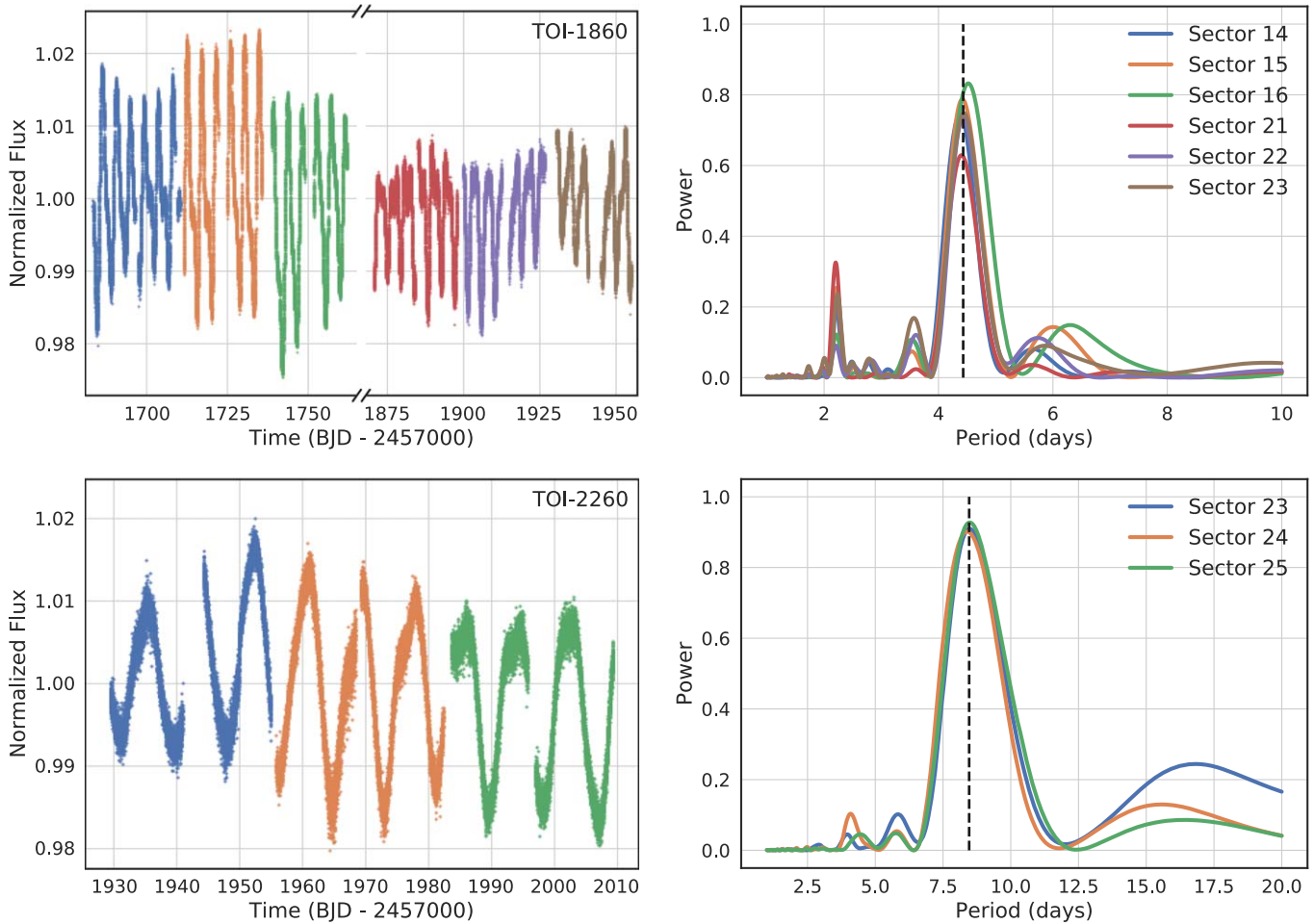
Figure 7. TESS light curves and Lomb–Scargle periodograms for TOI-1860 (top) and TOI-2260 (bottom). To estimate the rotation period of a star, we use the periodogram to calculate the peak period for each sector separately. Our estimate is then given by the mean and standard deviation of these rotation periods. For TOI-1860 and TOI-2260, we estimate a rotation period of 4.43 ± 0.04 days and 8.45 ± 0.06 days, respectively. These periods are indicated by vertical dashed lines in the right-hand panels.
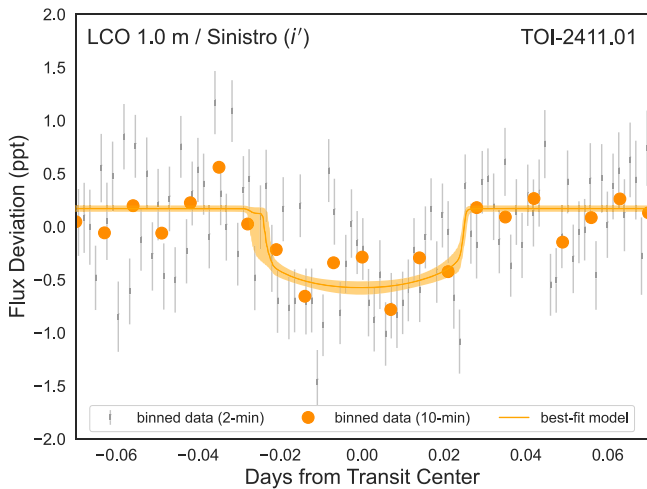
Figure 8. Phase-folded ground-based data and best-fit model of the transit of TOI-2411.01. The data is detrended with a linear model and 3σ outliers are removed.
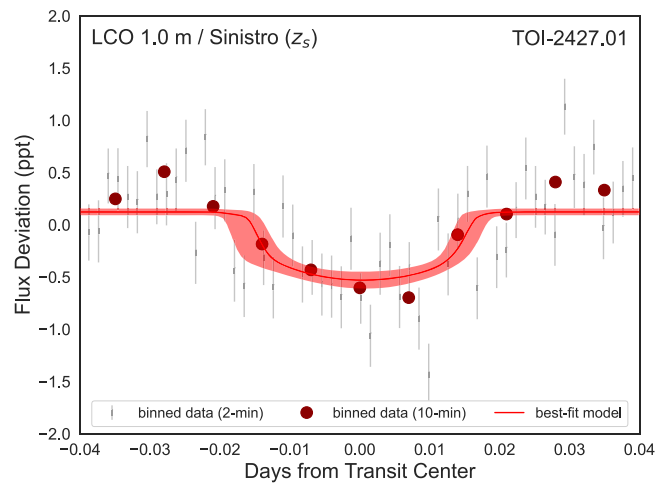
Figure 9. Phase-folded ground-based data and best-fit model of the transit of TOI-2427.01. The data are detrended with a linear model and 3σ outliers are removed.

Figure 10. Phase-folded ground-based data and best-fit model of the transit of TOI-2445.01. The data are detrended with a linear model and 3σ outliers are removed.

Scargle periodogram of the photometry from each TESS sector finds a maximum peak of 0.25, indicating that the star is quiet. This is corroborated by the low $v \sin i$ extracted from our TRES spectrum. TOI-544 has been observed in 2 TESS sectors (6 and 32).

Follow-up observations have found no evidence of this TOI being an FP. Time-series photometric follow-up of this TOI has cleared all neighboring stars as origins of the transit except for TIC 713009339 (located 5″26 south-southeast and 9.5 mag fainter in the TESS band) and TIC 50618707 (located 9″18 east-southeast and 6.9 mag fainter in the TESS band). TIC 713009339 is too faint to be the source of an astrophysical FP, but TIC 50618707 is not. We would like to note that the former of these nearby stars was detected by Gaia but not by 2MASS, while the latter was detected by 2MASS but not by Gaia. The parallaxes and proper motions of these two stars are unknown, so it is possible that they are the same star observed at two different epochs. If this were the case, the star would have been within the ~10″ × 10″ FOV of the Shane/ShARCS observations obtained on UT 2019 September 13, which reach contrasts of >8 mags in the K_s and J bands. However, no stars other than TIC 50618703 were detected in these observations. If this star (or stars, if they are indeed different sources) are really there, it (or they) would be far too faint to host eclipsing binaries mistakable for the TOI-544.01 transit. Regardless, we consider these two nearby stars in the remaining vetting steps for the sake of completeness.

The DAVE analysis of this TOI finds no strong indicators that the candidate is an FP. The SPOC data validation report for this TOI reports no significant centroid offset.

The TRICERATOPS analysis of this TOI finds FPP = $(8.25 \pm 0.91) \times 10^{-3}$ and NFPP = $(1.67 \pm 0.16) \times 10^{-16}$. This FPP and NFPP are sufficiently low to consider the planet validated. We hereafter refer to this planet as TOI-544 b.

We estimate the semiamplitude of the RV signal for this planet to be $K_{RV} = 3.2^{+2.4}_{-1.4}$ m s^{-1}, corresponding to $M_p = 5.0^{+4.0}_{-2.0} M_{\oplus}$.

5.5. TOI-731.01

TOI-731.01 is a $0.59 \pm 0.02 R_{\oplus}$ planet candidate with a 0.32 day orbital period orbiting a high-proper-motion ($\mu_{\alpha} = -462.5$ mas yr^{-1}, $\mu_{\delta} = -582.8$ mas yr^{-1}) M dwarf (TIC 34068865) that is 9.4 pc away and has a V magnitude of 10.15. A Lomb–Scargle periodogram of the photometry from each TESS sector finds a maximum peak of 0.07, indicating that the star is quiet. TOI-731 has been observed in three TESS sectors (9, 35, and 36).

Follow-up observations have found no evidence of this TOI being an FP. Time-series photometric follow-up of this TOI has

Table 9
Vetting Results

TOI	High-resolution Imaging	Recon Spectroscopy	Time-series Photometry	DAVE Results	FPP	NFPP	Validated
206.01	Clear	No data	Verified on target	Potential secondary eclipse	<0.01	<0.001	Y
500.01	Clear	Clear	All neighbors cleared	Clear but unreliable centroid analysis	<0.01	<0.001	Y
539.01	Clear	Clear	1 neighbor not cleared	Clear but unreliable centroid analysis	>0.01	<0.001	N
544.01	Clear	Clear	2 neighbors not cleared	Clear	<0.01	<0.001	Y
731.01	Clear	Clear	1 neighbor not cleared	Clear but unreliable centroid analysis	>0.01	<0.001	N
833.01	Clear	Clear	1 neighbor not cleared	Potential centroid offset	<0.01	<0.001	Y
1075.01	Clear	Clear	Verified on target	Clear	<0.01	<0.001	Y
1242.01	4″3 companion detected	Clear	1 neighbor not cleared	Potential centroid offset	<0.01	>0.001	N
1263.01	2″6 companion detected	Clear	2 neighbors not cleared	Different odd–even transit depths	>0.01	>0.001	N
1411.01	Clear	Clear	All neighbors cleared	Clear	<0.01	<0.001	Y
1442.01	Clear	No data	Verified on target	Clear but unreliable centroid analysis	<0.01	<0.001	Y
1693.01	Clear	Clear	Verified on target	Clear	<0.01	<0.001	Y
1860.01	Clear	Clear	1 neighbor not cleared	No results	<0.01	<0.001	Y
2260.01	Clear	Clear	All neighbors cleared	Clear	<0.01	<0.001	Y
2290.01	Clear	Clear	All neighbors cleared	Potential centroid offset	>0.01	<0.001	N
2411.01	Clear	Clear	Verified on target	No results	<0.01	<0.001	Y
2427.01	Clear	Clear	Verified on target	Potential centroid offset	<0.01	<0.001	Y
2445.01	Clear	No data	Verified on target	Clear but unreliable centroid analysis	<0.01	<0.001	Y

cleared all neighboring stars as transit sources except for TIC 34068883, which is 6.2 mag fainter in Gaia G_{Rp} and was 6″4 southwest at epoch 2020.361.[86] However, this follow-up has not detected the 0.24 ppt transit around the target star that is seen in the TESS data.

The DAVE analysis of this TOI finds no strong indicators that the candidate is an FP. Compared to TOI-500, the S/N of the per-transit difference images used by DAVE is even lower, and the measured centroids are unreliable. The SPOC data validation report for this TOI reports no significant centroid offset.

The TRICERATOPS analysis of this TOI finds FPP = $(1.89 \pm 0.46) \times 10^{-2}$ and NFPP = $(9.21 \pm 1.48) \times 10^{-26}$. This >1% FPP comes from the scenario that the TOI is a blended eclipsing binary. This FPP is too high to consider the planet candidate validated.

Assuming this is a real planet, we estimate the semiamplitude of the RV signal to be $K_{RV} = 0.22^{+0.11}_{-0.07}$ m s^{-1}, corresponding to $M_p = 0.15^{+0.07}_{-0.04} M_{\oplus}$.

5.6. TOI-833.01

TOI-833.01 is a $1.27 \pm 0.07 R_{\oplus}$ planet candidate with a 1.04 day orbital period orbiting a K dwarf (TIC 362249359) that is 41.7 pc away and has a V magnitude of 11.72. A Lomb–Scargle periodogram of the photometry from each TESS sector

finds a maximum peak of 0.20, indicating that the star is quiet. TOI-833 has been observed in 5 TESS sectors (9, 10, 11, 36, and 37).

Follow-up observations have found no evidence of this TOI being an FP. Time-series photometric follow-up of this TOI has made tentative detections of a ∼0.8–0.9 ppt transit on two different occasions. The field around this TOI is crowded, and it is not clear if the event is on target or due to blending with TIC 847323367 (located 3″1 north and 7.9 mag fainter in the TESS band).

The DAVE analysis of this TOI detects a potential centroid offset to the northeast but found no other indicators that this TOI is an FP. The SPOC data validation report for this TOI reports no significant centroid offset.

The TRICERATOPS analysis of this TOI finds FPP = $(2.32 \pm 0.23) \times 10^{-4}$ and NFPP = $(3.89 \pm 0.11) \times 10^{-10}$. This FPP and NFPP are sufficiently low to consider the planet validated. We hereafter refer to this planet as TOI-833 b. We estimate the semiamplitude of the RV signal for this planet to be $K_{RV} = 1.8^{+1.3}_{-0.5}$ m s^{-1}, corresponding to $M_p = 2.0^{+1.5}_{-0.6} M_{\oplus}$.

5.7. TOI-1075.01

TOI-1075.01 is a $1.72 \pm 0.08 R_{\oplus}$ planet candidate with a 0.60 day orbital period orbiting a K dwarf (TIC 351601843) that is 61.5 pc away and has a V magnitude of 12.62. A Lomb–Scargle periodogram of the photometry from each TESS sector finds a maximum peak of 0.02, indicating that the star is quiet. TOI-1075 has been observed in 2 TESS sectors (13 and 27).

Follow-up observations have found no evidence of this TOI being an FP. Time-series photometric follow-up has made

---

[86] This separation is continuing to decrease and will lead to a weak microlensing event with a closest approach of 510 mas in December 2028 (Bramich & Nielsen 2018). The event will not produce a brightening of more than 0.4 mmag but is predicted to produce an astrometric shift of 1 mas, possibly detectable by a future astrometric mission.

several detections of the transit of TOI-1075.01 on TIC 351601843 (shown in Figure 4).

The DAVE analysis of this TOI found no strong indicators that the candidate is an FP. The SPOC data validation report for this TOI reports no significant centroid offset.

The TRICERATOPS analysis of this TOI finds $FPP = (1.01 \pm 0.16) \times 10^{-3}$. Because TIC 351601843 has been verified as the host of the transit, TRICERATOPS finds $NFPP = 0.0$. This FPP is sufficiently low to consider the planet validated. We hereafter refer to this planet as TOI-1075 b.

We estimate the semiamplitude of the RV signal for this planet to be $K_{RV} = 4.3^{+2.9}_{-1.5}$ m s^{-1}, corresponding to $M_p = 4.0^{+2.7}_{-1.4} M_\oplus$.

5.8. TOI-1242.01

TOI-1242.01 is a $1.65 \pm 0.23 R_\oplus$ planet candidate with a 0.38 day orbital period orbiting a K dwarf (TIC 198212955) that is 110 pc away and has a V magnitude of 12.78. A Lomb–Scargle periodogram of the photometry from each TESS sector finds a maximum peak of 0.03, indicating that the star is quiet. This is corroborated by the low $v \sin i$ extracted from our TRES spectrum. TOI-1242 has been observed in 15 TESS sectors (14–26, 40, and 41) and is scheduled to be reobserved in another 8 sectors (48–55) between 2022 January 28 and 2022 September 1.

High-resolution imaging of this star detects TIC 198212956, a previously known star that is 4″3 north and 2.6 mag fainter in the TESS band but finds no other unresolved stars within detection limits. TIC 198212956 is almost certainly bound to TIC 198212955, due to their similar parallaxes and proper motions as reported by Gaia DR2. Spectroscopic observations confirm that the star is on the main sequence and rule out obvious spectroscopic binaries. Time-series photometric follow-up of this TOI has cleared all neighboring stars as origins of the transit except for TIC 198212956. The 0.6 ppt event seen in the TESS data has not been detected around the target star or its companion.

The DAVE analysis of this TOI detects a potential centroid offset to the northeast but finds no other indicators that this TOI is an FP. The SPOC data validation report for this TOI reports no significant centroid offset.

The TRICERATOPS analysis of this TOI finds $FPP = (3.36 \pm 0.17) \times 10^{-2}$ and $NFPP = (2.92 \pm 0.16) \times 10^{-2}$. These $>1\%$ FPP and NFPP are driven by the uncertainty over whether or not the transit originates from the target star or TIC 198212956. This FPP and NFPP are too high to consider this planet candidate validated.

Assuming this is a real planet around TIC 198212955, we estimate the semiamplitude of the RV signal to be $K_{RV} = 3.7^{+3.0}_{-1.7}$ m s^{-1}, corresponding to $M_p = 3.7^{+2.9}_{-1.5} M_\oplus$.

5.9. TOI-1263.01

TOI-1263.01 is a $1.36 \pm 0.16 R_\oplus$ planet candidate with a 1.02 day orbital period orbiting a K dwarf (TIC 406672232) that is 46.6 pc away and has a V magnitude of 9.36. A Lomb–Scargle periodogram of the photometry from each TESS sector finds a maximum peak of 0.12, indicating that the star is quiet. This is corroborated by the low $v \sin i$ extracted from our TRES and FIES spectra. TOI-1263 has been observed in three TESS sectors (14, 15, and 41) and is scheduled to be reobserved in another sector (55) between 2022 August 5 and 2022 September 1.

High-resolution imaging of this star detects TIC 1943945558, a previously known star that is 2″6 southeast and 3.6 mag fainter in the TESS band, but finds no other unresolved stars within detection limits. TIC 1943945558 is almost certainly bound to TIC 406672232 due to their similar parallaxes and proper motions as reported by Gaia DR2. Multiple spectroscopic observations confirm that the star is on the main sequence and rule out obvious spectroscopic binaries. Time-series photometric follow-up of this TOI has cleared all neighboring stars as origins of the transit except for TIC 1943945558 and TIC 1943945562, which is 9″1 northeast and 7.4 mag fainter in the TESS band. The 0.26 ppt event seen in the TESS data has not been detected around the target star.

The DAVE analysis of this TOI detects a potential difference between the even and odd primary transits, which could be indicative of an FP in the form of an eclipsing binary. DAVE did not report any other FP indicators for this TOI. The SPOC data validation report for this TOI reports no significant centroid offset.

The TRICERATOPS analysis of this TOI finds $FPP = (1.12 \pm 0.05) \times 10^{-2}$ and $NFPP = (1.04 \pm 0.05) \times 10^{-2}$. These $>1\%$ FPP and NFPP are driven by the uncertainty over whether or not the transit originates from the target star or TIC 1943945562. This FPP and NFPP are too high to consider this planet candidate validated.

Assuming this is a real planet around TIC 406672232, we estimate the semiamplitude of the RV signal to be $K_{RV} = 1.8^{+1.3}_{-0.7}$ m s^{-1}, corresponding to $M_p = 2.4^{+1.7}_{-0.8} M_\oplus$.

5.10. TOI-1411.01

TOI-1411.01 is a $1.36 \pm 0.16 R_\oplus$ planet candidate with a 1.45 day orbital period orbiting a K dwarf (TIC 116483514) that is 32.5 pc away and has a V magnitude of 10.51. A Lomb–Scargle periodogram of the photometry from each TESS sector finds a maximum peak of 0.02, indicating that the star is quiet. This is corroborated by the log $R'_{H K}$ of -4.7252 extracted from our HIRES spectrum and the low $v \sin i$ extracted from our TRES spectrum. TOI-1411 has been observed in three TESS sectors (16, 23, and 24) and is scheduled to be reobserved in another two sectors (50 and 51) between 2022 March 26 and 2022 May 18.

Follow-up observations have found no evidence of this TOI being an FP. Time-series photometric follow-up of this TOI has cleared all neighboring stars as origins of the transit. Of note to this TOI is TIC 1101969798, a periodic variable with a semiamplitude of 0.1 mag and a period of 0.107 days, which is located 90″ to the northeast.

The DAVE analysis of this TOI finds no strong indicators that the candidate is an FP. The SPOC data validation report for this TOI reports no significant centroid offset.

The TRICERATOPS analysis of this TOI finds $FPP = (1.18 \pm 0.68) \times 10^{-4}$. Because all neighboring stars have been cleared, TRICERATOPS finds $NFPP = 0.0$. This FPP is sufficiently low to consider the planet validated. We hereafter refer to this planet as TOI-1411 b.

We estimate the semiamplitude of the RV signal for this planet to be $K_{RV} = 2.0^{+1.7}_{-1.0}$ m s^{-1}, corresponding to $M_p = 2.5^{+2.0}_{-1.1} M_\oplus$. D. Vermilion et al. (2021, in preparation), who detect the RV signal of this planet, reports a K_{RV} 5σ upper limit of 4.26 m s^{-1} (or a mass of $5.66 M_\oplus$), consistent with our estimate and with a terrestrial composition.

5.11. TOI-1442.01

TOI-1442.01 is a $1.17 \pm 0.06\,R_\oplus$ planet candidate with a 0.41 day orbital period orbiting an M dwarf (TIC 235683377) that is 41.2 pc away and has a V magnitude of 15.39. A Lomb–Scargle periodogram of the photometry from each TESS sector finds a maximum peak of 0.02, indicating that the star is quiet. TOI-1442 has been observed in 15 TESS sectors (14–26, 40, and 41) and is scheduled to be reobserved in another 9 sectors (47–55) between 2021 December 30 and 2022 September 1.

Follow-up observations have found no evidence of this TOI being an FP, although no spectroscopic observations of this TOI have been collected. Time-series photometric follow-up has made several detections of the transit of TOI-1442.01 on TIC 235683377 (shown in Figure 5).

The DAVE analysis of this TOI finds no strong indicators that the candidate is an FP. However, the S/N of the per-transit difference images used by DAVE is very low, and the measured centroids are unreliable. The SPOC data validation report for this TOI reports no significant centroid offset.

The TRICERATOPS analysis of this TOI finds FPP $= (7.00 \pm 4.11) \times 10^{-6}$. Because the transit has been verified on target, TRICERATOPS finds NFPP $= 0.0$. This FPP is sufficiently low to consider the planet validated. We hereafter refer to this planet as TOI-1442 b.

We estimate the semiamplitude of the RV signal for this planet to be $K_{RV} = 3.2^{+2.2}_{-1.0}$ m s^{-1}, corresponding to $M_p = 1.6^{+1.1}_{-0.5}\,M_\oplus$.

5.12. TOI-1693.01

TOI-1693.01 is a $1.42 \pm 0.10\,R_\oplus$ planet candidate with a 1.77 day orbital period orbiting an M dwarf (TIC 353475866) that is 30.8 pc away and has a V magnitude of 12.96. A Lomb–Scargle periodogram of the photometry from each TESS sector finds a maximum peak of 0.01, indicating that the star is quiet. This is corroborated by the $\log R'_{H\,K}$ of -5.2169 extracted from our HIRES spectrum. TOI-1693 has been observed in four TESS sectors (19 and 43–45).

Follow-up observations have found no evidence of this TOI being an FP. Time-series photometric follow-up has made several detections of the transit of TOI-1693.01 on TIC 353475866 (shown in Figure 6).[87]

The DAVE analysis of this TOI finds no strong indicators that the candidate is an FP. The SPOC data validation report for this TOI reports no significant centroid offset.

The TRICERATOPS analysis of this TOI finds FPP $= (1.47 \pm 0.13) \times 10^{-3}$. Because the transit has been verified on target, TRICERATOPS finds NFPP $= 0.0$. This FPP is sufficiently low to consider the planet validated. We hereafter refer to this planet as TOI-1693 b.

We estimate the semiamplitude of the RV signal for this planet to be $K_{RV} = 2.4^{+1.9}_{-0.8}$ m s^{-1}, corresponding to $M_p = 2.8^{+2.2}_{-1.0}\,M_\oplus$.

5.13. TOI-1860.01

TOI-1860.01 is a $1.31 \pm 0.04\,R_\oplus$ planet candidate with a 1.07 day orbital period orbiting a G dwarf (TIC 202426247) that is 45.9 pc away and has a V magnitude of 8.4. A Lomb–Scargle periodogram of the photometry from each TESS sector finds a maximum peak of 0.83, indicating strong activity and a

young host star. We also estimate a $\log R'_{H\,K}$ of -4.2524 from our HIRES spectrum, which indicates that the star is young and active. TOI-1860 has been observed in seven TESS sectors (14–16, 21–23, and 41) and is scheduled to be reobserved in another three sectors (48–50) between 2022 January 28 and 2022 April 22.

Because this is an active star, we can use the TESS light curve to derive its rotation period. In Figure 7, we display the results of a Lomb–Scargle periodogram applied to each sector separately, which gives a rotation period of 4.43 ± 0.06 days. Using the relation defined in Barnes (2007), we estimate the age of the star to be 133 ± 26 Myr. Lastly, we use BANYAN Σ (Gagné et al. 2018) to determine the probability that the star is a member of a nearby young association. This analysis returns a 99.9% probability that TOI-1860 is a field star.

Another interesting aspect of TOI-1860 is that it has stellar parameters and a metallicity very similar to that of the Sun and qualifies as a solar twin according to most definitions (de Strobel 1996; Ramírez et al. 2014). For solar twins, there is known to be a strong correlation between [Y/Mg] and stellar age (Nissen 2015; Maia et al. 2016). Because we obtained elemental abundances for this star using KeckSpec (see Table 6), we are able to conduct an independent check of the age of this system. Using the relation provided in Maia et al. (2016) and [Y/Mg] $= 0.196 \pm 0.090$, we estimate an age upper limit of 1.93 Gyr, which is consistent with our estimation based on gyrochronology.

Follow-up observations have found no evidence of this TOI being an FP. Time-series photometric follow-up of this TOI has cleared all neighboring stars as origins of the transit except for TIC 1102367690, which is $5\rlap{.}''5$ west and 5.8 mag fainter in the TESS band. The 0.23 ppt event seen in the TESS data has not been detected around the target star.

DAVE was unable to perform a vetting analysis of this TOI, due to a failure of its transit model to fit the TESS data. The SPOC data validation report for this TOI reports no significant centroid offset.

The TRICERATOPS analysis of this TOI find FPP $= (1.97 \pm 0.45) \times 10^{-4}$ and NFPP $= (9.68 \pm 2.23) \times 10^{-6}$. This FPP and NFPP are sufficiently low to consider the planet validated. We hereafter refer to this planet as TOI-1860 b.

We estimate the semiamplitude of the RV signal for this planet to be $K_{RV} = 1.4^{+0.8}_{-0.4}$ m s^{-1}, corresponding to $M_p = 2.2^{+1.3}_{-0.7}\,M_\oplus$.

5.14. TOI-2260.01

TOI-2260.01 is a $1.62 \pm 0.13\,R_\oplus$ planet candidate with a 0.35 day orbital period orbiting a G dwarf (TIC 232568235) that is 101.3 pc away and has a V magnitude of 10.47. A Lomb–Scargle periodogram of the photometry from each TESS sector finds a maximum peak of 0.93, indicating strong activity and a young host star. We also estimate a $\log R'_{H\,K}$ of -4.438 from our HIRES spectrum, which indicates that the star is young and active. TOI-2260 has been observed in three TESS sectors (23–25) and is scheduled to be reobserved in another three sectors (50–52) between 2022 March 26 and 2022 June 13.

Because this is an active star, we can use the TESS light curve to derive its rotation period. In Figure 7, we display the results of a Lomb–Scargle periodogram applied to each sector separately, which gives a rotation period of 8.45 ± 0.03 days. Using the relation defined in Barnes (2007), we estimate the age of the star to be 321 ± 96 Myr. Lastly, we use BANYAN Σ (Gagné et al. 2018) to determine the probability that the star is a

---

[87] Those observations are blended with TIC 723362263, which is $3\rlap{.}''75$ southwest and 8.3 mag fainter in the TESS band, which is marginally too faint to have caused the TESS detection.

member of a nearby young association. This analysis returns a 99.9% probability that TOI-2260 is a field star.

Follow-up observations have found no evidence of this TOI being an FP. Time-series photometric follow-up of this TOI has cleared all neighboring stars as origins of the transit.

The DAVE analysis of this TOI finds no strong indicators that the candidate is an FP. The SPOC data validation report for this TOI reports a significant centroid offset in sector 24 but has not conducted centroid offset analyses for sectors 23 and 25. However, given that all neighboring stars have been cleared from being nearby eclipsing binaries, this offset is unlikely to be caused by an FP coming from a nearby star.

The TRICERATOPS analysis of this TOI finds FPP = $(5.26 \pm 0.50) \times 10^{-3}$. Because all neighboring stars have been cleared, TRICERATOPS finds NFPP = 0.0. This FPP is sufficiently low to consider the planet validated. We hereafter refer to this planet as TOI-2260 b.

We estimate the semiamplitude of the RV signal for this planet to be $K_{RV} = 3.0^{+2.2}_{-1.1}$ m s^{-1}, corresponding to $M_p = 3.5^{+2.5}_{-1.3} M_\oplus$.

5.15. TOI-2290.01

TOI-2290.01 is a $1.17 \pm 0.07 R_\oplus$ planet candidate with a 0.39 day orbital period orbiting a K dwarf (TIC 321688498) that is 58.1 pc away and has a V magnitude of 12.64. A Lomb–Scargle periodogram of the photometry from each TESS sector finds a maximum peak of 0.03, indicating that the star is quiet. However, the $\log R'_{H K}$ of -4.459 extracted from our HIRES spectrum suggests that the star may actually be quite active. TOI-2290 has been observed in four TESS sectors (17, 18, 24, and 25).

Follow-up observations have found no evidence of this TOI being an FP. Time-series photometric follow-up of this TOI has cleared all neighboring stars as origins of the transit.

The DAVE analysis of this TOI finds a potential centroid offset but finds no other significant FP indicators. No data validation reports have been generated by the SPOC pipeline for this TOI.

The TRICERATOPS analysis of this TOI finds FPP = $(4.92 \pm 0.11) \times 10^{-1}$. Because all neighboring stars have been cleared, TRICERATOPS finds NFPP = 0.0. The reason for this >1% FPP comes from the scenario that the TOI is a blended eclipsing binary. This FPP is too high to consider the planet validated.

Assuming this is a real planet, we estimate the semiamplitude of the RV signal to be $K_{RV} = 2.1^{+1.7}_{-0.7}$ m s^{-1}, corresponding to $M_p = 1.6^{+1.4}_{-0.6} M_\oplus$.

5.16. TOI-2411.01

TOI-2411.01 is a $1.68 \pm 0.11 R_\oplus$ planet candidate with a 0.78 day orbital period orbiting a K dwarf (TIC 10837041) that is 59.5 pc away and has a V magnitude of 11.27. A Lomb–Scargle periodogram of the photometry from each TESS sector finds a maximum peak of 0.002, indicating that the star is quiet. TOI-2411 has been observed in two TESS sectors (3 and 30).

Follow-up observations have found no evidence of this TOI being an FP. Time-series photometric follow-up has made several detections of the transit of TOI-2411.01 on TIC 10837041 (shown in Figure 8).

DAVE is unable to analyze this TOI due to the very low S/N of the data. The SPOC data validation report for this TOI reports no significant centroid offset or any other FP indicators.

The TRICERATOPS analysis of this TOI finds FPP = $(1.17 \pm 0.05) \times 10^{-3}$. Because transits have been verified on target, TRICERATOPS finds NFPP = 0.0. This FPP is sufficiently low to consider the planet validated. We hereafter refer to this planet as TOI-2411 b.

We estimate the semiamplitude of the RV signal for this planet to be $K_{RV} = 3.6^{+2.5}_{-1.3}$ m s^{-1}, corresponding to $M_p = 3.9^{+2.8}_{-1.4} M_\oplus$.

5.17. TOI-2427.01

TOI-2427.01 is a $1.80 \pm 0.12 R_\oplus$ planet candidate with a 1.31 day orbital period orbiting a K dwarf (TIC 142937186) that is 28.5 pc away and has a V magnitude of 10.30. A Lomb–Scargle periodogram of the photometry from each TESS sector finds a maximum peak of 0.05, indicating that the star is quiet. TOI-2427 has been observed in one TESS sector (31).

Follow-up observations have found no evidence of this TOI being an FP. Time-series photometric follow-up has made several detections of the transit of TOI-2427.01 on TIC 142937186 (shown in Figure 9).

The DAVE analysis of this TOI finds a potential centroid offset but finds no other indicators that this TOI is an FP. The SPOC data validation report for this TOI also reports a significant centroid offset. However, given that all neighboring stars have been cleared from being nearby eclipsing binaries, this offset is unlikely to be caused by an FP originating from a nearby star.

The TRICERATOPS analysis of this TOI finds FPP = $(7.35 \pm 2.72) \times 10^{-3}$. Because transits have been verified on target, TRICERATOPS finds NFPP = 0.0. This FPP is sufficiently low to consider the planet validated. We hereafter refer to this planet TOI-2427 b.

We estimate the semiamplitude of the RV signal for this planet to be $K_{RV} = 3.2^{+2.4}_{-1.2}$ m s^{-1}, corresponding to $M_p = 4.1^{+3.1}_{-1.5} M_\oplus$.

5.18. TOI-2445.01

TOI-2445.01 is a $1.25 \pm 0.08 R_\oplus$ planet candidate with a 0.37 day orbital period orbiting an M dwarf (TIC 439867639) that is 48.6 pc away and has a V magnitude of 15.69. A Lomb–Scargle periodogram of the photometry from each TESS sector finds a maximum peak of 0.04, indicating that the star is quiet. TOI-2445 has been observed in two TESS sectors (4 and 31).

Follow-up observations have found no evidence of this TOI being an FP, although no spectroscopic observations of this TOI have been collected. Time-series photometric follow-up has made several detections of the transit of TOI-2445.01 on TIC 439867639 (shown in Figure 10).

The DAVE analysis of this TOI finds no strong indicators that the candidate is an FP. However, like TOI-739, the S/N of the per-transit difference images used by DAVE is very low and the measured centroids are unreliable. No data validation reports have been generated by the SPOC pipeline for this TOI.

The TRICERATOPS analysis of this TOI finds FPP = $(1.88 \pm 0.45) \times 10^{-4}$. Because transits have been verified on target, TRICERATOPS finds NFPP = 0.0. This FPP is sufficiently low to consider the planet validated. We hereby refer to this planet as TOI-2445 b.
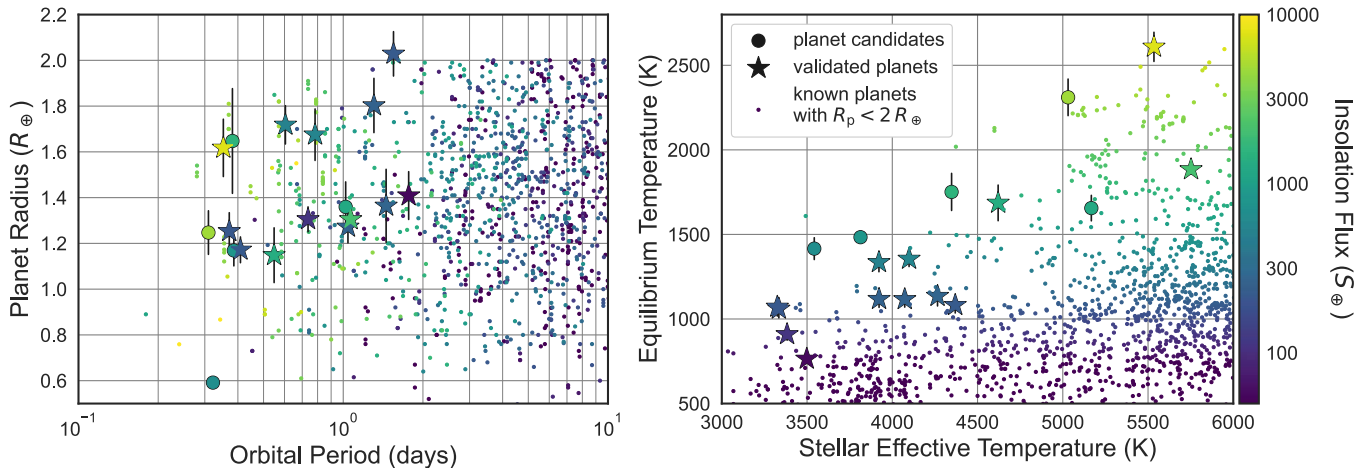
Figure 11. Left: planet radii and orbital periods of all planet candidates (circles) and validated planets (stars) in this paper, along with all known planets with $R_p < 2 R_\oplus$ (points). Right: planet equilibrium temperatures and host star effective temperatures for the same planet candidates, validated planets, and known planets. Color indicates insolation flux. Data for known planets were obtained through the NASA Exoplanet Archive.

We estimate the semiamplitude of the RV signal for this planet to be $K_{RV} = 4.5^{+2.8}_{-1.7}$ m s^{-1}, corresponding to $M_p = 2.0^{+1.2}_{-0.7} M_\oplus$.

6. Discussion

In Section 5, we scrutinized the available data of 18 potentially terrestrial TESS planet candidates that display promise as subjects of emission spectroscopy observations with JWST. Of these, 13 were validated. In Figure 11, we show how our targets are distributed in the planet radius–orbital period plane and the planet equilibrium temperature–stellar effective temperature plane with all other known planets with $R_p < 2 R_\oplus$ included for reference.

The planet candidates and planets analyzed in this paper cover a wide region of parameter space that will allow for studies of hot, potentially terrestrial planets across different environments. For instance, many of the planets validated in this paper are among the hottest known planets with $R_p < 2 R_\oplus$. For stars with $T_{eff} < 3500$ K, TOI-1442 b and TOI-206 b rank as the fifth and sixth hottest planets, respectively, with $T_{eq} = 1072 \pm 54$ K and $T_{eq} = 910 \pm 36$ K, only being surpassed by GJ 1252 b ($T_{eq} \sim 1089$ K; Shporer et al. 2020), K2-137 b ($T_{eq} \sim 1608$ K; Smith et al. 2018), TOI-1634 b ($T_{eq} \sim 1608$ K; Cloutier et al. 2021), and TOI-1685 b ($T_{eq} \sim 1066$ K; Bluhm et al. 2021). For stars with $3500 < T_{eff} < 4000$ K, TOI-1075 b and TOI-833 b are the first and second hottest planets, respectively, with $T_{eq} = 1336 \pm 56$ K and $T_{eq} = 1118 \pm 49$ K, but would be superseded by TOI-2290.01 if found to be a bona fide planet. Lastly, TOI-2260 b is the fourth hottest known planet of this size to orbit any star, with $T_{eq} = 2609 \pm 86$ K, only being surpassed by KOI-55 b ($T_{eq} \sim 8000$ K; Charpinet et al. 2011), TOI-55 c ($T_{eq} \sim 7000$ K; Charpinet et al. 2011), and Kepler-1340 b ($T_{eq} \sim 2860$ K; Morton et al. 2016). All of these planets will be valuable for studying the evolution of planets with high equilibrium temperatures, which is a key parameter in core-powered atmospheric mass-loss models for small planets (Ginzburg et al. 2016, 2018).

Of our 13 validated planets, 7 (TOI-206 b, TOI-500 b, TOI-1075 b, TOI-1442 b, TOI-2260 b, TOI-2411 b, and TOI-2445 b) are ultra-short-period planets, which are named for their <1 day orbital periods (e.g., Léger et al. 2009; Batalha et al. 2011; Sanchis-Ojeda et al. 2013). One interesting case is that of

TOI-2260 b, whose star we determine to have a metallicity of [Fe/H] = 0.22 ± 0.06 dex. While an ultra-short-period planet orbiting such a metal-rich star is not unheard of, other planets of this type tend to orbit stars with lower metallicities (Winn et al. 2017). Specifically, according to the NASA Exoplanet Archive,[88] fewer than 10% of ultra-short-period planets orbit stars with metallicities greater than 0.2 dex. Further characterization of these planets could be helpful for understanding how these planets form around stars of different metal contents.

For TOI-1860 b and TOI-2260 b, we were able to use the TESS light curves of their host stars to estimate their ages, which we found to be 133 ± 26 and 321 ± 96 Myr, respectively. These ages make the planets some of the youngest known transiting planets to date. In addition to the recently validated TOI-1807 b, a ~$1.82 R_\oplus$ planet that was found to have an age of 180 ± 40 by Hedges et al. (2021), these planets will be important case studies for determining how terrestrial planets evolve in hot environments. Specifically, they will allow us to test two competing theories behind the existence and behavior of the radius gap. Photoevaporative atmospheric mass loss (Jackson et al. 2012; Lopez & Fortney 2013; Owen & Wu 2013; Jin et al. 2014; Owen & Wu 2017; Jin & Mordasini 2018) predicts small planets to be stripped of their atmospheres within the first ~100 Myr of the system lifetime when the host star is still active enough to produce the high-energy photons responsible for atmospheric escape (Ribas et al. 2005; Jackson et al. 2012). Conversely, core-powered atmospheric mass loss is predicted to occur over a steadier ~1 Gyr timescale (Gupta & Schlichting 2019). Some studies have explored this distinction by examining how the occurrence rate gap evolves over Gyr timescales (Berger et al. 2020; David et al. 2021; Sandoval et al. 2021). By characterizing these planets further, either by measuring their masses or observing their emission spectra with JWST, we will be able to determine to what extent these planets have experienced atmospheric mass loss over their short lives. Observations that support the lack of an atmosphere around these planets would provide evidence for the former, while observations that support the existence of atmospheres would provide evidence for the latter.

---

[88] https://exoplanetarchive.ipac.caltech.edu/

Table 10
Confirmed and Validated Planets with $R_p < 2\,R_\oplus$ and ESM > 7.5

TOI	Alt Name	K_s mag	T_{eff} (K)	P_{orb} (days)	R_p ($R_\oplus$)	M_p ($M_\oplus$)	T_{eq} (K)	ESM	Confirmation/Validation Paper
134.01	L 168-9 b	7.082 ± 0.031	3800 ± 70	1.401500 ± 0.000180	1.39 ± 0.09	4.60 ± 0.56	981 ± 27	9.9 ± 1.4	Astudillo-Defru et al. (2020)
136.01	LHS 3844 b	9.145 ± 0.023	3036 ± 77	0.462929 ± 0.000002	1.30 ± 0.02	...	805 ± 27	28.8 ± 1.8	Vanderspek et al. (2019)
141.01	HD 213885 b	6.419 ± 0.024	5978 ± 50	1.008035 ± 0.000020	1.75 ± 0.05	8.83 ± 0.66	2131 ± 21	14.1 ± 0.8	Espinoza et al. (2020)
396.01	HR 858 c	5.149 ± 0.020	6201 ± 50	5.972930 ± 0.000600	1.94 ± 0.07	...	1317 ± 16	9.7 ± 0.7	Vanderburg et al. (2019)
431.02	HIP 26013 b	6.723 ± 0.021	4850 ± 75	0.490047 ± 0.000010	1.28 ± 0.04	3.07 ± 0.35	1888 ± 50	16.0 ± 1.2	Osborn et al. 2021 (submitted)
667.01	GJ 1132 b	8.322 ± 0.027	3270 ± 140	1.628931 ± 0.000027	1.13 ± 0.06	1.66 ± 0.23	584 ± 30	9.5 ± 1.4	Berta-Thompson et al. (2015)[a]
732.01	LTT 3780 b	8.204 ± 0.021	3331 ± 157	0.768448 ± 0.000054	1.33 ± 0.07	2.62 ± 0.47	892 ± 44	13.4 ± 1.6	Cloutier et al. (2020)
836.02	HIP 73427 b	6.804 ± 0.018	4250 ± 120	3.816514 ± 0.000757	1.81 ± 0.27	5.76 ± 1.14	834 ± 47	8.7 ± 2.7	Teske et al. (2021)
1078.01	GJ 1252 b	7.915 ± 0.023	3458 ± 140	0.518235 ± 0.000006	1.19 ± 0.07	2.09 ± 0.56	1089 ± 53	16.3 ± 2.2	Shporer et al. (2020)
1416.01	HIP 70705 b	7.708 ± 0.024	4884 ± 70	1.069763 ± 0.000005	1.73 ± 0.05	5.00 ± 1.10	1514 ± 24	11.0 ± 0.7	H. J. Deeg et al. (2021, in preparation)
1462.01	HD 158259 b	4.965 ± 0.023	5801 ± 157	2.178000 ± 0.000100	1.25 ± 0.10[b]	2.22 ± 0.42	1673 ± 76	8.4 ± 1.5	Hara et al. (2020)
1469.01	HD 219134 b	3.261 ± 0.304	4699 ± 16	3.093500 ± 0.000300	1.60 ± 0.06	4.74 ± 0.19	1014 ± 8	37 ± 6	Motalebi et al. (2015)
1469.02	HD 219134 c	3.261 ± 0.304	4699 ± 16	6.764580 ± 0.000330	1.51 ± 0.05	4.36 ± 0.22	782 ± 6	18.3 ± 2.9	Gillon et al. (2017a)
1773.01	55 Cnc e	4.015 ± 0.036	5172 ± 18	0.736547 ± 0.000001	1.88 ± 0.03	7.99 ± 0.33	1947 ± 13	69.9 ± 2.7	McArthur et al. (2004),winn2011super[c]
1634.01	TOI-1634 b	8.600 ± 0.014	3550 ± 69	0.989343 ± 0.000015	1.79 ± 0.08	4.91 ± 0.69	923 ± 23	13.9 ± 1.3	Cloutier et al. (2021)[d]
1685.01	TOI-1685 b	8.758 ± 0.020	3434 ± 51	0.6691403 ± 0.000002	1.70 ± 0.07	3.78 ± 0.63	1066 ± 24	13.8 ± 1.2	Bluhm et al. (2021)[d]
1807.01	HIP 65469 b	7.568 ± 9.995[e]	4757 ± 50	0.549372 ± 0.000007	1.82 ± 0.05	...	1730 ± 28	22.6 ± 1.4	Hedges et al. (2021)
1827.01	GJ 486 b	6.362 ± 0.018	3340 ± 54	1.467119 ± 0.000031	1.31 ± 0.07	2.82 ± 0.12	700 ± 17	21.5 ± 2.4	Trifonov et al. (2021)
2431.01	HIP 11707 b	7.554 ± 0.023	4079 ± 126	0.224200 ± 0.000020	1.62 ± 0.21	...	2048 ± 125	29 ± 8	L. Malavolta et al. (2021, in preparation)[f]
...	HD 3167 b	7.066 ± 0.020	5261 ± 60	0.959641 ± 0.000012	1.70 ± 0.17	5.02 ± 0.38	1746 ± 46	14.0 ± 2.9	Vanderburg et al. (2016); Christiansen et al. (2017)
...	K2-141 b	8.401 ± 0.023	4599 ± 79	0.280324 ± 0.000002	1.51 ± 0.05	5.08 ± 0.41	2115 ± 48	15.0 ± 1.1	Malavolta et al. (2018)
...	GJ 9827 b	7.193 ± 0.024	4340 ± 47	1.208982 ± 0.000007	1.58 ± 0.03	4.91 ± 0.49	1183 ± 15	14.9 ± 0.6	Niraula et al. (2017); Rodriguez et al. (2018)[g]

Notes.
[a] Listed host star and planet properties from Bonfils et al. (2018).
[b] Planet radius was calculated using the transit depth listed on ExoFOP-TESS, $\delta = 90 \pm 7$ ppm.
[c] Listed host star and planet properties from Bourrier et al. (2018).
[d] Also confirmed by Hirano et al. (2021), who find the mass of TOI-1634 b to be about twice what is listed here.
[e] The large uncertainty in this K_s mag is reported by 2MASS. The 2MASS J and H mag are 8.103 ± 0.023 and 7.605 ± 0.018, respectively.
[f] Entries for this row are taken from TICv8 and ExoFOP-TESS, as the authors of this paper were unable to share exact figures at the time of writing. The mass of the transiting object has been measured and is consistent with that of a planet (via private communication).
[g] Listed host star and planet properties from Rice et al. (2019).
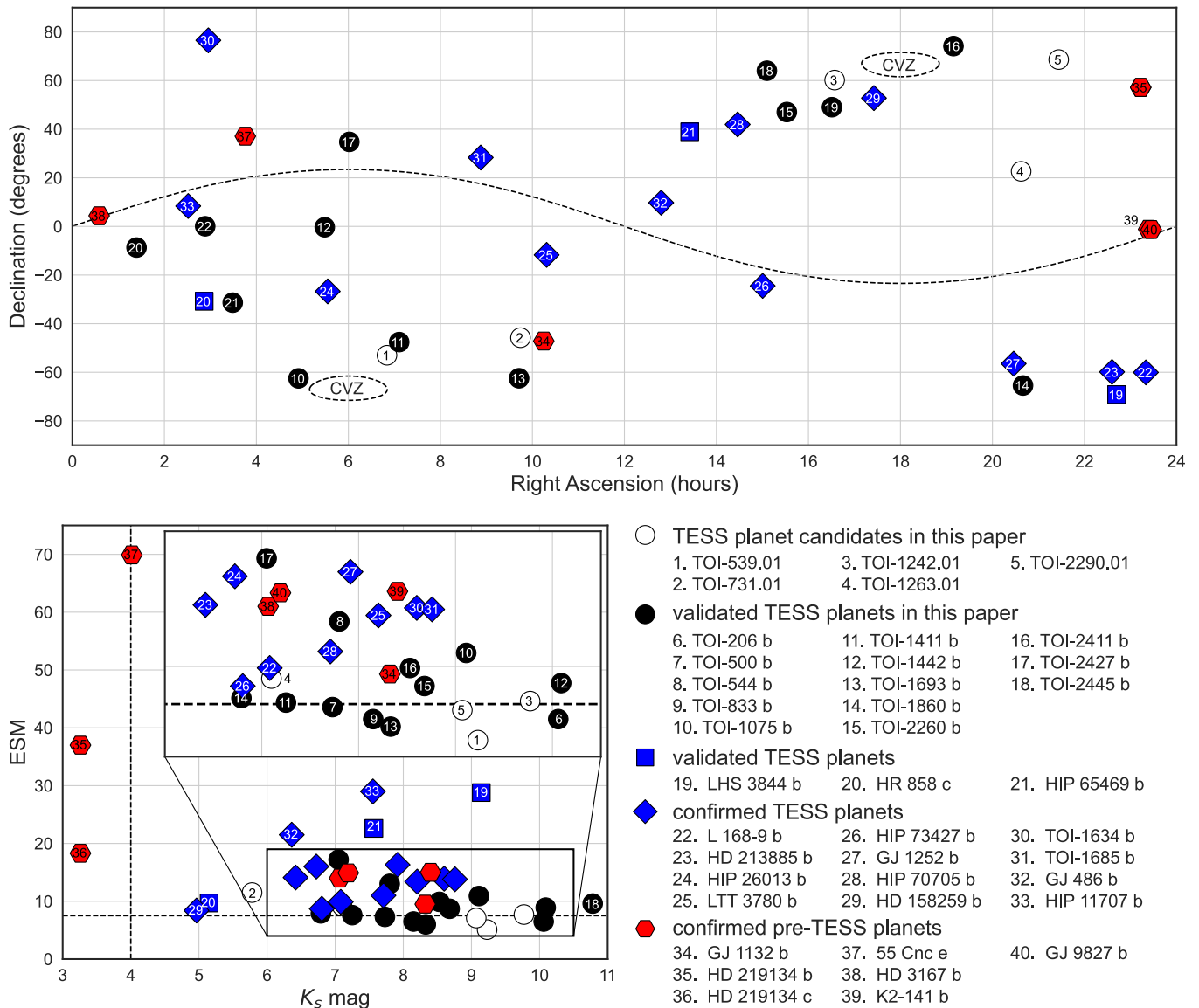
Figure 12. Top: coordinates of the TESS planet candidates in this paper (white circles), validated TESS planets in this paper (black circles), validated TESS planets (blue squares), confirmed TESS planets (blue diamonds), and confirmed pre-TESS planets (red hexagons). The ecliptic plane and ecliptic poles (i.e., the JWST continuous viewing zones) are shown as dashed black lines. Bottom: emission spectroscopy metric versus apparent K_s magnitude for each planet candidate and planet. The dashed lines indicate the minimum values a target should have to be observed with JWST.

As was mentioned in Section 5.13, TOI-1860 is also a solar twin. With an age of 133 ± 26 Myr, this star is the youngest solar twin with a transiting planet discovered yet. Future studies of this system could shed light on the formation and evolution of planets around Sun-like stars.

The last notable feature of the targets included in this paper is that they span a wide range of stellar spectral types. It is believed that the radius at which short-period planets transition from having volatile-rich atmospheres to having terrestrial-like or negligible atmospheres depends on the mass of the host star. Specifically, Fulton & Petigura (2018) found evidence that this transition radius increases with increasing stellar mass. In other words, a $1.6\,R_{\oplus}$ planet has a higher probability of having a volatile-rich atmosphere when orbiting a K dwarf than it does when orbiting a G dwarf. Because our sample spans from low-mass M dwarfs to Sun-like stars, acquiring emission

spectroscopy observations of our targets would allow for a direct test of this hypothesis.

To explore how the TESS mission has thus far increased the number of potentially terrestrial planets amenable to emission spectroscopy observations, we compile a list of all terrestrial planets with ESM > 7.5 that were confirmed (i.e., have had their masses measured with precise radial velocities) or validated (i.e., have had their planetary natures certified using methods that do not involve a mass measurement) prior to the writing of this paper. Table 10 shows the host and planet properties of these systems, which were identified using the NASA Exoplanet Archive. Of these, 7 were discovered and confirmed prior to the TESS mission, 12 were discovered by TESS and subsequently confirmed, and 3 were discovered by TESS and subsequently validated. Going by these numbers, TESS has increased the number of potential JWST emission

spectroscopy targets from 7 to 22. If we include the planets validated in this paper, this count increases to 35—a five-fold increase in the size of the sample available prior to TESS.

Another aspect one must consider when planning for JWST observations of these targets is their locations in the sky. JWST operates in an ecliptic coordinate framework that makes the telescope capable of observing targets within $5°$ of the north and south ecliptic poles (regions dubbed the "continuous viewing zones," or CVZs) at any time of the year and all other regions of the sky twice per year over time intervals that vary with ecliptic longitude. In other words, targets at or near the ecliptic poles will be observable for longer periods of time than targets near the ecliptic plane. In the top panel of Figure 12, we show the position of each planet candidate and confirmed/ validated planet in our sample. Though no targets lie within the CVZs, several targets (e.g., TOI-206, TOI-500, TOI-539, TOI-1242, TOI-1442, and HD 158259) are only a short distance away. While most of the systems in our sample would make excellent targets for these observations, those close to the CVZs would allow for more flexibility when planning observations.

Lastly, in addition to ESM, there are other properties of these systems that must be considered when planning for JWST observations. For instance, a star that is too bright in the passband could saturate the instrument in the minimum number of groups (two) required for a JWST observation.[89] A vast majority of terrestrial planet emission spectroscopy observations will be conducted using MIRI LRS, a low-resolution spectrograph with a wavelength range of 5–12 μm. `PandExo` (Batalha et al. 2017, 2019), a tool created to calculate the optimal exposure times for exoplanetary JWST observations, estimates the brightest star one can observe with MIRI LRS without saturating to have $K \sim 4$. All of the planet candidates discussed in Section 5 meet this criterion, and all but three previously confirmed/validated planets (HD 219134 b, HD 219134 c, and 55 Cnc e) meet this criterion. This indicates that nearly all planets in our sample will be observable with this instrument. The location of each planet candidate and confirmed/validated planet in ESM–K mag space is shown in the bottom panel of Figure 12.

7. Conclusion

We vet 18 hot TESS planet candidates that are potentially terrestrial ($R_p < 2 R_\oplus$) and would make good targets for emission spectroscopy observations with JWST (ESM $\gtrsim$ 7.5) using several follow-up observations from the TFOP and analyses performed with `DAVE` and `TRICERATOPS`. Of these 18, 13 were validated.

The 13 validated planets exist in a diverse set of environments that will allow for differential studies of small planets in and around the 1.5–2.0 $R_\oplus$ radius gap. Some key takeaways about these validated planets are as follows:

- Seven of the validated planets (TOI-206 b, TOI-500 b, TOI-1075 b, TOI-1442 b, TOI-2260 b, TOI-2411 b, and TOI-2445 b) are ultra-short-period planets.
- TOI-1860 b is a 1.34 $R_\oplus$ planet orbiting a young (133 ± 26 Myr) solar twin. This is the youngest planetary system discovered around a solar twin to date.

---

[89] A "group" is JWST terminology for the number of consecutively read frames with no resets.

- TOI-2260 b is a 1.68 $R_\oplus$ ultra-short-period planet orbiting a young (321 ± 96 Myr) late G dwarf. With a stellar metallicity of $[Fe/H] = 0.22 \pm 0.06$ dex, this star ranks among the most metal-rich to host an ultra-short-period planet. TOI-2260 b has a T_{eq} of 2609 ± 86 K and is the fourth hottest planet with $R_p < 2 R_\oplus$ discovered to date.

Lastly, we assemble a list of all other previously discovered transiting planets that met our selection criteria for being ideal JWST emission spectroscopy targets. We discuss the prospects of using JWST to observe each of these known planets, along with the planet candidates and validated planets discussed in this paper.

ORCID iDs

Steven Giacalone https://orcid.org/0000-0002-8965-3969
Courtney D. Dressing https://orcid.org/0000-0001-8189-0233
Christina Hedges https://orcid.org/0000-0002-3385-8391
Veselin B. Kostov https://orcid.org/0000-0001-9786-1031
Karen A. Collins https://orcid.org/0000-0001-6588-9574
Eric L. N. Jensen https://orcid.org/0000-0002-4625-7333
Daniel A. Yahalomi https://orcid.org/0000-0003-4755-584X
Allyson Bieryla https://orcid.org/0000-0001-6637-5401
David R. Ciardi https://orcid.org/0000-0002-5741-3047
Steve B. Howell https://orcid.org/0000-0002-2532-2853
Jorge Lillo-Box https://orcid.org/0000-0003-3742-1987
Khalid Barkaoui https://orcid.org/0000-0003-1464-9276
Jennifer G. Winters https://orcid.org/0000-0001-6031-9513
Elisabeth Matthews https://orcid.org/0000-0003-0593-1560
John H. Livingston https://orcid.org/0000-0002-4881-3620
Samuel N. Quinn https://orcid.org/0000-0002-8964-8377
Boris S. Safonov https://orcid.org/0000-0003-1713-3208
Charles Cadieux https://orcid.org/0000-0001-9291-5555
E. Furlan https://orcid.org/0000-0001-9800-6248
Avi M. Mandell https://orcid.org/0000-0002-8119-3355
Emily A. Gilbert https://orcid.org/0000-0002-0388-8004
Ethan Kruse https://orcid.org/0000-0002-0493-1342
Elisa V. Quintana https://orcid.org/0000-0003-1309-2904
George R. Ricker https://orcid.org/0000-0003-2058-6662
S. Seager https://orcid.org/0000-0002-6892-6948
Joshua N. Winn https://orcid.org/0000-0002-4265-047X
Jon M. Jenkins https://orcid.org/0000-0002-4715-9460
David Baker https://orcid.org/0000-0002-2970-0532
Thomas Barclay https://orcid.org/0000-0001-7139-2724
David Barrado https://orcid.org/0000-0002-5971-9242
Natalie M. Batalha https://orcid.org/0000-0002-7030-9519
Alexander A. Belinski https://orcid.org/0000-0003-3469-0989
Zouhair Benkhaldoun https://orcid.org/0000-0001-6285-9847
Lars A. Buchhave https://orcid.org/0000-0003-1605-5666
Luca Cacciapuoti https://orcid.org/0000-0001-8266-0894
David Charbonneau https://orcid.org/0000-0002-9003-484X

Ashley Chontos ⓘ https://orcid.org/0000-0003-1125-2564
Jessie L. Christiansen ⓘ https://orcid.org/0000-0002-8035-4778
Ryan Cloutier ⓘ https://orcid.org/0000-0001-5383-9393
Kevin I. Collins ⓘ https://orcid.org/0000-0003-2781-3207
Dennis M. Conti ⓘ https://orcid.org/0000-0003-2239-0567
René Doyon ⓘ https://orcid.org/0000-0001-5485-4675
Mohammed El Mufti ⓘ https://orcid.org/0000-0001-8364-2903
Emma Esparza-Borges ⓘ https://orcid.org/0000-0002-2341-3233
Zahra Essack ⓘ https://orcid.org/0000-0002-2482-0180
Akihiko Fukui ⓘ https://orcid.org/0000-0002-4909-5763
Tianjun Gan ⓘ https://orcid.org/0000-0002-4503-9705
Kaz Gary ⓘ https://orcid.org/0000-0002-9106-7301
Michaël Gillon ⓘ https://orcid.org/0000-0003-1462-7739
Eric Girardin ⓘ https://orcid.org/0000-0002-5443-3640
Ana Glidden ⓘ https://orcid.org/0000-0002-5322-2315
Erica J. Gonzales ⓘ https://orcid.org/0000-0002-9329-2190
Elliott P. Horch ⓘ https://orcid.org/0000-0003-2159-1463
Krzysztof G. Hełminiak ⓘ https://orcid.org/0000-0002-7650-3603
Andrew W. Howard ⓘ https://orcid.org/0000-0001-8638-0320
Daniel Huber ⓘ https://orcid.org/0000-0001-8832-4488
Emmanuël Jehin ⓘ https://orcid.org/0000-0001-8923-488X
Taiki Kagetani ⓘ https://orcid.org/0000-0002-5331-6637
Stephen R. Kane ⓘ https://orcid.org/0000-0002-7084-0529
Kiyoe Kawauchi ⓘ https://orcid.org/0000-0003-1205-5108
John F. Kielkopf ⓘ https://orcid.org/0000-0003-0497-2651
Pablo Lewin ⓘ https://orcid.org/0000-0003-0828-6368
Michael B. Lund ⓘ https://orcid.org/0000-0003-2527-1598
Shude Mao ⓘ https://orcid.org/0000-0001-8317-2788
Bob Massey ⓘ https://orcid.org/0000-0001-8879-7138
Rachel A. Matson ⓘ https://orcid.org/0000-0001-7233-7508
Ismael Mireles ⓘ https://orcid.org/0000-0002-4510-2268
Mayuko Mori ⓘ https://orcid.org/0000-0003-1368-6593
Felipe Murgas ⓘ https://orcid.org/0000-0001-9087-1245
Norio Narita ⓘ https://orcid.org/0000-0001-8511-2981
Erik A. Petigura ⓘ https://orcid.org/0000-0003-0967-2893
Alex S. Polanski ⓘ https://orcid.org/0000-0001-7047-8681
Francisco J. Pozuelos ⓘ https://orcid.org/0000-0003-1572-7707
Enric Palle ⓘ https://orcid.org/0000-0003-0987-1593
Hannu Parviainen ⓘ https://orcid.org/0000-0001-5519-1391
Peter P. Plavchan ⓘ https://orcid.org/0000-0002-8864-1667
Paul Robertson ⓘ https://orcid.org/0000-0003-0149-9678
Mark E. Rose ⓘ https://orcid.org/0000-0003-4724-745X
Pamela Rowden ⓘ https://orcid.org/0000-0002-4829-7101
Arpita Roy ⓘ https://orcid.org/0000-0001-8127-5775
Arjun B. Savel ⓘ https://orcid.org/0000-0002-2454-768X
Joshua E. Schlieder ⓘ https://orcid.org/0000-0001-5347-7062
Richard P. Schwarz ⓘ https://orcid.org/0000-0001-8227-1020
Aleksandra Selezneva ⓘ https://orcid.org/0000-0002-4900-5713
Chris Stockdale ⓘ https://orcid.org/0000-0003-2163-1437
Ivan A. Strakhov ⓘ https://orcid.org/0000-0003-0647-6133
Thiam-Guan Tan ⓘ https://orcid.org/0000-0001-5603-6895
Guillermo Torres ⓘ https://orcid.org/0000-0002-5286-0251
René Tronsgaard ⓘ https://orcid.org/0000-0003-1001-0707
Joseph D. Twicken ⓘ https://orcid.org/0000-0002-6778-7552
Ian A. Waite ⓘ https://orcid.org/0000-0002-3249-3538
Yujie Zou ⓘ https://orcid.org/0000-0002-5609-4427

References

Ansdell, M., Ioannou, Y., Osborn, H. P., et al. 2018, ApJL, 869, L7
Astudillo-Defru, N., Cloutier, R., Wang, S., et al. 2020, A&A, 636, A58
Barkaoui, K., Burdanov, A., Hellier, C., et al. 2019, AJ, 157, 43
Barnes, S. A. 2007, ApJ, 669, 1167
Barros, S., Almenara, J., Deleuil, M., et al. 2014, A&A, 569, A74
Batalha, N. E., Mandell, A., Pontoppidan, K., et al. 2017, PASP, 129, 064501
Batalha, N. E., Mandell, A., Pontoppidan, K., et al. 2019, Pandexo: Instrument simulations for exoplanet observations planning, Astrophysics Source Code Library, ascl:1906.016
Batalha, N. M., Borucki, W. J., Bryson, S. T., et al. 2011, ApJ, 729, 27
Benedict, G., Henry, T., Franz, O., et al. 2016, AJ, 152, 141
Berger, T. A., Huber, D., Gaidos, E., van Saders, J. L., & Weiss, L. M. 2020, AJ, 160, 108
Berta-Thompson, Z. K., Irwin, J., Charbonneau, D., et al. 2015, Natur, 527, 204
Bluhm, P., Pallé, E., Molaverdikhani, K., et al. 2021, A&A, 650, A78
Bond, J. C., O'Brien, D. P., & Lauretta, D. S. 2010, ApJ, 715, 1050
Bonfils, X., Almenara, J.-M., Cloutier, R., et al. 2018, A&A, 618, A142
Bourrier, V., Dumusque, X., Dorn, C., et al. 2018, A&A, 619, A1
Bramich, D. M., & Nielsen, M. B. 2018, AcA, 68, 183
Brown, T. M., Baliber, N., Bianco, F. B., et al. 2013, PASP, 125, 1031
Buchhave, L. A., Dressing, C. D., Dumusque, X., et al. 2016, AJ, 152, 160
Buchhave, L. A., Latham, D., Johansen, A., et al. 2012, Natur, 486, 375
Carter, J. A., Agol, E., Chaplin, W. J., et al. 2012, Sci, 337, 556
Charpinet, S., Fontaine, G., Brassard, P., et al. 2011, Natur, 480, 496
Chen, J., & Kipping, D. 2016, ApJ, 834, 17
Christiansen, J. L., Vanderburg, A., Burt, J., et al. 2017, AJ, 154, 122
Ciardi, D. R., Beichman, C. A., Horch, E. P., & Howell, S. B. 2015, ApJ, 805, 16
Cloutier, R., Charbonneau, D., Stassun, K. G., et al. 2021, AJ, 162, 79
Cloutier, R., Eastman, J. D., Rodriguez, J. E., et al. 2020, AJ, 160, 3
Cloutier, R., & Menou, K. 2020, AJ, 159, 211
Collins, K. A., Kielkopf, J. F., Stassun, K. G., & Hessman, F. V. 2017, AJ, 153, 77
David, T. J., Contardo, G., Sandoval, A., et al. 2020, AJ, 161, 265
David, T. J., Contardo, G., Sandoval, A., et al. 2021, AJ, 161, 265
de Strobel, G. C. 1996, A&ARv, 7, 243
Dekany, R., Roberts, J., Burruss, R., et al. 2013, ApJ, 776, 130
Demory, B.-O., Gillon, M., De Wit, J., et al. 2016, Natur, 532, 207
Dragomir, D., Matthews, J. M., Eastman, J. D., et al. 2013, ApJL, 772, L2
Dressing, C. D., Charbonneau, D., Dumusque, X., et al. 2015, ApJ, 800, 135
Espinoza, N., Brahm, R., Henning, T., et al. 2020, MNRAS, 491, 2982
Essack, Z., Seager, S., & Pajusalu, M. 2020, ApJ, 898, 160
Fűrész, G. 2008, PhD thesis, Univ. of Szeged, Hungary
Foreman-Mackey, D., Savel, A., Luger, R., et al. 2021, exoplanet-dev/exoplanet v0.4.5, Zenodo, doi:10.5281/zenodo.1998447
Fortney, J. J., Marley, M. S., & Barnes, J. W. 2007, ApJ, 659, 1661
Fried, D. L. 1978, JOSA, 68, 1651
Fulton, B. J., & Petigura, E. A. 2018, AJ, 156, 264
Fulton, B. J., Petigura, E. A., Howard, A. W., et al. 2017, AJ, 154, 109
Furlan, E., Ciardi, D., Everett, M., et al. 2017, AJ, 153, 71
Gagné, J., Mamajek, E. E., Malo, L., et al. 2018, ApJ, 856, 23
Garcia, L. J., Timmermans, M., Pozuelos, F. J., et al. 2021, MNRAS, 509, 4817
Gavel, D., Kupke, R., Dillon, D., et al. 2014, Proc. SPIE, 9148, 914805
Giacalone, S., & Dressing, C. D. 2020, triceratops: Candidate exoplanet rating tool, Astrophysics Source Code Library, ascl:2002.004
Giacalone, S., Dressing, C. D., Jensen, E. L. N., et al. 2021, AJ, 161, 24
Gillon, M., Demory, B.-O., Van Grootel, V., et al. 2017a, NatAs, 1, 1
Gillon, M., Jehin, E., Magain, P., et al. 2011, EPJ Web of Conf., 11, 06002
Gillon, M., Triaud, A. H., Demory, B.-O., et al. 2017b, Natur, 542, 456
Ginzburg, S., Schlichting, H. E., & Sari, R. 2016, ApJ, 825, 29
Ginzburg, S., Schlichting, H. E., & Sari, R. 2018, MNRAS, 476, 759
Grasset, O., Schneider, J., & Sotin, C. 2009, ApJ, 693, 722
Greene, T. P., Line, M. R., Montero, C., et al. 2016, ApJ, 817, 17
Guerrero, N. M., Seager, S., Huang, C. X., et al. 2021, ApJS, 254, 39
Gupta, A., & Schlichting, H. E. 2019, MNRAS, 487, 24
Hara, N., Bouchy, F., Stalport, M., et al. 2020, A&A, 636, L6
Hayward, T., Brandl, B., Pirger, B., et al. 2001, PASP, 113, 105
Hedges, C., Angus, R., Barentsen, G., et al. 2020, RNAAS, 4, 220
Hedges, C., Hughes, A., Zhou, G., et al. 2021, AJ, 162, 54
Hillenbrand, L., Isaacson, H., Marcy, G., et al. 2014, arXiv:1408.3475
Hirano, T., Livingston, J. H., Fukui, A., et al. 2021, AJ, 162, 161
Hirsch, L. A., Ciardi, D. R., Howard, A. W., et al. 2017, AJ, 153, 117
Horch, E., Dinescu, D., Girard, T., et al. 1996, AJ, 111, 1681
Horch, E. P., Howell, S. B., Everett, M. E., & Ciardi, D. R. 2012, AJ, 144, 165
Horch, E. P., Veillette, D. R., Baena Gallé, R., et al. 2009, AJ, 137, 5057

Hormuth, F., Brandner, W., Hippler, S., & Henning, T. 2008, JPhCS, 131, 012051

Howard, A. W., Johnson, J. A., Marcy, G. W., et al. 2010, ApJ, 721, 1467

Howell, S. B., Everett, M. E., Sherry, W., Horch, E., & Ciardi, D. R. 2011, AJ, 142, 19

Hu, R., Ehlmann, B. L., & Seager, S. 2012, ApJ, 752, 7

Irwin, J. M., Berta-Thompson, Z. K., Charbonneau, D., et al. 2015, in 18th Cambridge Workshop on Cool Stars, Stellar Systems, and the Sun, ed. G. van Belle & H. C. Harris (Cambridge, MA: Lowell Observatory), 767

Jackson, A. P., Davis, T. A., & Wheatley, P. J. 2012, MNRAS, 422, 2024

Jehin, E., Gillon, M., Queloz, D., et al. 2011, Msngr, 145, 2

Jenkins, J. M. 2002, ApJ, 575, 493

Jenkins, J. M., Chandrasekaran, H., McCauliff, S. D., et al. 2010, Proc. SPIE, 7740, 77400D

Jenkins, J. M., Twicken, J. D., McCauliff, S., et al. 2016, Proc. SPIE, 9913, 99133E

Jensen, E. 2013, Tapir: A web interface for transit/eclipse observability, Astrophysics Source Code Library, ascl:1306.007

Jin, S., & Mordasini, C. 2018, ApJ, 853, 163

Jin, S., Mordasini, C., Parmentier, V., et al. 2014, ApJ, 795, 65

Kaltenegger, L., MacDonald, R. J., Kozakis, T., et al. 2020, ApJL, 901, L1

Kempton, E. M.-R., Bean, J. L., Louie, D. R., et al. 2018, PASP, 130, 114401

Kipping, D. M. 2013, MNRAS, 435, 2152

Kite, E. S., Fegley, Bruce, J., Schaefer, L., & Gaidos, E. 2016, ApJ, 828, 80

Kolbl, R., Marcy, G. W., Isaacson, H., & Howard, A. W. 2014, AJ, 149, 18

Koll, D. D., & Abbot, D. S. 2016, ApJ, 825, 99

Koll, D. D. B., Malik, M., Mansfield, M., et al. 2019, ApJ, 886, 140

Konopacky, Q. M., Barman, T. S., Macintosh, B. A., & Marois, C. 2013, Sci, 339, 1398

Kostov, V. B., Mullally, S. E., Quintana, E. V., et al. 2019, AJ, 157, 124

Kreidberg, L., Koll, D. D., Morley, C., et al. 2019, Natur, 573, 87

Kreidberg, L., & Loeb, A. 2016, ApJL, 832, L12

Kupke, R., Gavel, D., Roskosi, C., et al. 2012, Proc. SPIE, 8447, 84473G

Kurucz, R. L. 1993, SYNTHE Spectrum Synthesis Programs and Line Data (Cambridge, MA: Smithsonian Astrophysical Observatory)

Lee, E. J., & Chiang, E. 2016, ApJ, 817, 90

Lee, E. J., Chiang, E., & Ormel, C. W. 2014, ApJ, 797, 95

Léger, A., Rouan, D., Schneider, J., et al. 2009, A&A, 506, 287

Li, J., Tenenbaum, P., Twicken, J. D., et al. 2019, PASP, 131, 024506

Lightkurve Collaboration, Cardoso, J. V. d. M., Hedges, C., et al. 1812, Lightkurve: Kepler and TESS time series analysis in Python, Astrophysics Source Code Library, ascl:1812.013

Lillo-Box, J., Barrado, D., & Bouy, H. 2012, A&A, 546, A10

Lillo-Box, J., Barrado, D., & Bouy, H. 2014, A&A, 566, A103

Lincowski, A. P., Meadows, V. S., Crisp, D., et al. 2018, ApJ, 867, 76

Linsky, J., Worden, S., McClintock, W., & Robertson, R. 1979, ApJS, 41, 47

Lopez, E. D., & Fortney, J. J. 2013, ApJ, 776, 2

Lopez, E. D., & Rice, K. 2018, MNRAS, 479, 5303

Luger, R., & Barnes, R. 2015, AsBio, 15, 119

Lund, M. B., & Ciardi, D. 2020, AAS Meeting, 52, 249.06

Lustig-Yaeger, J., Meadows, V. S., & Lincowski, A. P. 2019, AJ, 158, 27

Maia, M. T., Ramírez, I., Meléndez, J., et al. 2016, A&A, 590, A32

Malavolta, L., Mayo, A. W., Louden, T., et al. 2018, AJ, 155, 107

Mann, A. W., Dupuy, T., Kraus, A. L., et al. 2019, ApJ, 871, 63

Mann, A. W., Feiden, G. A., Gaidos, E., Boyajian, T., & von Braun, K. 2015, ApJ, 804, 64

Mansfield, M., Kite, E. S., Hu, R., et al. 2019, ApJ, 886, 141

Martinez, C. F., Cunha, K., Ghezzi, L., & Smith, V. V. 2019, ApJ, 875, 29

McArthur, B. E., Endl, M., Cochran, W. D., et al. 2004, ApJL, 614, L81

McCully, C., Volgenau, N. H., Harbeck, D.-R., et al. 2018, Proc. SPIE, 10707, 107070K

Moriarty, J., Madhusudhan, N., & Fischer, D. 2014, ApJ, 787, 81

Morley, C. V., Kreidberg, L., Rustamkulov, Z., Robinson, T., & Fortney, J. J. 2017, ApJ, 850, 121

Morris, R. L., Twicken, J. D., Smith, J. C., et al. 2020, Kepler Science Document KSCI, 19081-003, 6

Morton, T. D. 2012, ApJ, 761, 6

Morton, T. D., Bryson, S. T., Coughlin, J. L., et al. 2016, ApJ, 822, 86

Motalebi, F., Udry, S., Gillon, M., et al. 2015, A&A, 584, A72

Narita, N., Fukui, A., Kusakabe, N., et al. 2015, JATIS, 1, 045001

Narita, N., Fukui, A., Kusakabe, N., et al. 2019, JATIS, 5, 015001

Narita, N., Fukui, A., Yamamuro, T., et al. 2020, Proc. SPIE, 11447, 114475K

Niraula, P., Redfield, S., Dai, F., et al. 2017, AJ, 154, 266

Nissen, P. E. 2015, A&A, 579, A52

Nutzman, P., & Charbonneau, D. 2008, PASP, 120, 317

Owen, J. E., & Wu, Y. 2013, ApJ, 775, 105

Owen, J. E., & Wu, Y. 2017, ApJ, 847, 29

Petigura, E. A. 2015, PhD thesis, Univ. of California, Berkeley

Ramírez, I., Meléndez, J., Bean, J., et al. 2014, A&A, 572, A48

Ribas, I., Guinan, E. F., Güdel, M., & Audard, M. 2005, ApJ, 622, 680

Rice, K., Malavolta, L., Mayo, A., et al. 2019, MNRAS, 484, 3731

Rice, M., & Brewer, J. M. 2020, ApJ, 898, 119

Ricker, G. R., Latham, D., Vanderspek, R., et al. 2010, BAAS, 42, 459

Rodriguez, J. E., Vanderburg, A., Eastman, J. D., et al. 2018, AJ, 155, 72

Rogers, L. A. 2015, ApJ, 801, 41

Rouan, D., Deeg, H. J., Demangeon, O., et al. 2011, ApJL, 741, L30

Safonov, B., Lysenko, P., & Dodin, A. 2017, AstL, 43, 344

Samuel, B., Leconte, J., Rouan, D., et al. 2014, A&A, 563, A103

Sanchis-Ojeda, R., Rappaport, S., Winn, J. N., et al. 2013, ApJ, 774, 54

Sandoval, A., Contardo, G., & David, T. J. 2021, ApJ, 911, 117

Savel, A. B., Dressing, C. D., Hirsch, L. A., et al. 2020, AJ, 160, 287

Schaefer, L., Lodders, K., & Fegley, B. 2012, ApJ, 755, 41

Schlichting, H. E., Sari, R., & Yalinewich, A. 2015, Icar, 247, 81

Schwarz, G. 1978, AnSta, 6, 461

Scott, N. J., & Howell, S. B. 2018, Proc. SPIE, 10701, 107010G

Scott, N. J., Howell, S. B., Horch, E. P., & Everett, M. E. 2018, PASP, 130, 054502

Seager, S., & Deming, D. 2009, ApJ, 703, 1884

Seager, S., Kuchner, M., Hier-Majumder, C., & Militzer, B. 2007, ApJ, 669, 1279

Selsis, F., Wordsworth, R., & Forget, F. 2011, A&A, 532, A1

Shallue, C. J., & Vanderburg, A. 2018, AJ, 155, 94

Shporer, A., Collins, K. A., Astudillo-Defru, N., et al. 2020, ApJL, 890, L7

Shuvalov, V. 2009, M&PS, 44, 1095

Smith, A., Cabrera, J., Csizmadia, S., et al. 2018, MNRAS, 474, 5523

Smith, J. C., Stumpe, M. C., Van Cleve, J. E., et al. 2012, PASP, 124, 1000

Stassun, K. G., Oelkers, R. J., Pepper, J., et al. 2018, AJ, 156, 102

Strehl, K. 1902, AN, 158, 89

Stumpe, M. C., Smith, J. C., Catanzarite, J. H., et al. 2014, PASP, 126, 100

Stumpe, M. C., Smith, J. C., Van Cleve, J. E., et al. 2012, PASP, 124, 985

Telting, J. H., Avila, G., Buchhave, L., et al. 2014, AN, 335, 41

Teske, J., Wang, S. X., Wolfgang, A., et al. 2021, ApJ, 256, 33

Teske, J. K., Ciardi, D. R., Howell, S. B., Hirsch, L. A., & Johnson, R. A. 2018, AJ, 156, 292

Tokovinin, A., Fischer, D. A., Bonati, M., et al. 2013, PASP, 125, 1336

Trifonov, T., Caballero, J., Morales, J., et al. 2021, Sci, 371, 1038

Twicken, J. D., Catanzarite, J. H., Clarke, B. D., et al. 2018, PASP, 130, 064502

Twicken, J. D., Clarke, B. D., Bryson, S. T., et al. 2010, Proc. SPIE, 7740, 774023

Valencia, D., O'Connell, R. J., & Sasselov, D. 2006, Icar, 181, 545

Valencia, D., Sasselov, D. D., & O'Connell, R. J. 2007a, ApJ, 665, 1413

Valencia, D., Sasselov, D. D., & O'Connell, R. J. 2007b, ApJ, 656, 545

Van Eylen, V., Agentoft, C., Lundkvist, M., et al. 2018, MNRAS, 479, 4786

Vanderburg, A., Bieryla, A., Duev, D. A., et al. 2016, ApJL, 829, L9

Vanderburg, A., Huang, C. X., Rodriguez, J. E., et al. 2019, ApJL, 881, L19

Vanderspek, R., Huang, C. X., Vanderburg, A., et al. 2019, ApJL, 871, L24

Vogt, S., Allen, S., Bigelow, B., et al. 1994, Proc. SPIE, 2198, 362

Winn, J. N., Matthews, J. M., Dawson, R. I., et al. 2011, ApJL, 737, L18

Winn, J. N., Sanchis-Ojeda, R., Rogers, L., et al. 2017, AJ, 154, 60

Wu, Y. 2019, ApJ, 874, 91

Yee, S. W., Petigura, E. A., & von Braun, K. 2017, ApJ, 836, 77

Yi, S., Demarque, P., Kim, Y.-C., et al. 2001, ApJS, 136, 417

Zeng, L., & Sasselov, D. 2013, PASP, 125, 227

Zeng, L., Sasselov, D. D., & Jacobsen, S. B. 2016, ApJ, 819, 127

Zeng, L., & Seager, S. 2008, PASP, 120, 983

Ziegler, C., Tokovinin, A., Briceño, C., et al. 2019, AJ, 159, 19

Ziegler, C., Tokovinin, A., Latiolais, M., et al. 2021, AJ, 162, 192

Zilinskas, M., Miguel, Y., Mollière, P., & Tsai, S.-M. 2020, MNRAS, 494, 1490